
Spectroscopic and theoretical study of dipole moments of alkali dimers

Andreas Gerdes

January 2010

Fakultät für Mathematik und Physik
Gottfried Wilhelm Leibniz Universität Hannover

Faculté des Sciences
Université Paris-Sud XI

Spectroscopic and theoretical study of dipole moments of alkali dimers

Von der Fakultät für Mathematik und Physik der
Gottfried Wilhelm Leibniz Universität Hannover

zur Erlangung des Grades

Doktor der Naturwissenschaften
Dr. rer. nat.

genehmigte Dissertation
von

Dipl.-Phys. Andreas Gerdes
geboren am 18.04.1978 in Wilhelmshaven

2010

Promotion durchgeführt als *Cotutelle* an den Instituten

Laboratoire Aimé Cotton, CNRS,
Université Paris Sud XI
Bât 505 Campus d'Orsay
91405 Orsay Cedex
Frankreich

und

Institut für Quantenoptik
Gottfried Wilhelm Leibniz Universität Hannover
Welfengarten 1
30175 Hannover
Deutschland

Referent:	Prof. Dr. Eberhard Tiemann
Koreferent:	Dr. Olivier Dulieu
Prüfer:	Prof. Dr. Joachim Großer
	Prof. Dr. Milutin Kovacev
	Dr. Amanda Ross
	Dr. Jacques Robert

Tag der Promotion: 26.01.2010

Thèse

Présentée pour obtenir

LE GRADE DE DOCTEUR EN SCIENCES
DE L'UNIVERSITÉ PARIS-SUD XI

Spécialité: Physique
École doctorale: Ondes et Matière

par
Andreas GERDES

Spectroscopic and theoretical study of dipole
moments of alkali dimers

Thèse préparée en cotutelle à

Laboratoire Aimé Cotton, CNRS,
Université Paris Sud XI
Bât 505 Campus d'Orsay
91405 Orsay Cedex
France

et

Institut für Quantenoptik
Gottfried Wilhelm Leibniz Universität Hannover
Welfengarten 1
30175 Hanovre
Allemagne

Soutenue le 26 janvier 2010 devant la commission d'examen

Jury: Dr. Olivier Dulieu (Directeur de thèse)
Dr. Jacques Robert
Dr. Amanda Ross (Rapporteur)
Prof. Dr. Eberhard Tiemann (Co-Directeur de thèse, Rapporteur)
Prof. Dr. Milutin Kovacev
Prof. Dr. Joachim Großer

Abstract

Andreas Gerdes

Spectroscopic and theoretical study of dipole moments of alkali dimers

This thesis is concerned with the theoretical and experimental investigation of alkali dimers. Results of *ab initio* calculations will be illustrated with the molecules Cs_2 and NaK . The complete set of potential energy curves of the six lowest states of Cs_2 for each symmetry was calculated and the improvement in long-range behaviour will be shown. Transition dipole moments and permanent electric dipole moments can be determined; the final set of wave functions enables the calculation of the corresponding eigenvalues. For NaK permanent electric dipole moments are given for certain electronic states.

In a heatpipe for NaK light induced fluorescence is spectrally resolved with a Fourier-transform spectrometer. The observed spectra allow for a joint description of the electronic singlet and triplet ground states.

A molecular beam apparatus for heteronuclear dimers has been built from scratch and is characterized by means of K_2 and NaK measurements. Excitation spectroscopy of the NaK dimer helps to find suitable transitions for a Stark spectroscopy. Permanent electric dipole moments of the polar NaK molecule are determined experimentally for two states and the findings are compared to the *ab initio* predictions.

Keywords:

Laser spectroscopy, Quantum chemistry calculations, Stark effect

Zusammenfassung

Andreas Gerdes

Spektroskopische and theoretische Bestimmung der Dipolmomente von Alkalidimeren

Im Rahmen dieser Arbeit wurden verschiedene Alkalidimere theoretisch und experimentell untersucht. Die Ergebnisse der *ab initio* Berechnungen werden anhand der Beispiele Cs_2 und NaK vorgestellt. Sie liefern erstmals einen kompletten Satz der Potentialkurven der untersten sechs Zustände des Cs_2 für jede Symmetrie. Zusätzlich zu den Potentialkurven sind aber auch Übergangsmatrixelemente und permanente elektrische Dipolmomente aus der Berechnung heraus zugänglich, denn wenn man die elektronische Schrödingergleichung des Problems gelöst hat, und alle Wellenfunktionen vorliegen, sind nur noch die entsprechenden Erwartungswerte für die gesuchten elektronischen Größen zu bilden. Für das NaK -Molekül liefert die Rechnung permanente elektrische Dipolmomente für verschiedene elektronische Zustände.

In einer Gaszelle wurde bei fester Laseranregung des NaK -Moleküls die entstehende Fluoreszenz mit Hilfe eines Fourier-Transform-Spektrometers spektral zerlegt. Die gewonnenen Spektren ermöglichen eine Beschreibung der elektronischen Grundzustände im Singulett- und Triplett-System, wobei der Fokus auf der gemeinsamen Beschreibung beider Grundzustände liegt.

Eine Molekülstrahlapparatur für heteronukleare Moleküle wurde komplett neu aufgebaut und mit den Molekülen K_2 und NaK charakterisiert. Mittels Anregungsspektroskopie wurde das NaK -Molekül weiter untersucht und passende Übergänge für die sich anschließende Stark-Spektroskopie gefunden. Das permanente elektrische Dipolmoment des polaren Moleküls NaK wurde experimentell für zwei elektronische Zustände bestimmt und mit den Vorhersagen aus den *ab initio* Rechnungen verglichen.

Schlagwörter:

Laserspektroskopie, Quantenchemie-Berechnungen, Starkeffekt

Résumé

Andreas Gerdes

Etude spectroscopique et théorique des moments dipolaires de dimères d'alcalins

L'objet de cette thèse est l'étude théorique et expérimentale des dimères d'alcalins. Les résultats des calculs *ab initio* sont présentés pour les molécules Cs_2 et NaK . La série de courbes d'énergie potentielle des six premiers états de Cs_2 pour chaque symétrie a été calculée et les améliorations du comportement à longue portée sont montrées. Les moments dipolaires de transition et les moments dipolaires électriques permanents ont été déterminés; la série finale de fonctions d'ondes permet le calcul des valeurs propres correspondantes. Les moments dipolaires électriques permanents de NaK sont donnés pour certains états électroniques.

Dans un calorimètre à NaK la fluorescence induite par lumière est spectralement résolue avec un spectromètre à transformée de Fourier. Le spectre observé permet une description conjointe du singulet électronique et des états triplets fondamentaux.

Un appareil à faisceau moléculaire pour les dimères hétéronucléaires a été fabriqué à partir de zéro et caractérisé avec des mesures de K_2 et NaK . La spectroscopie par excitation du dimère NaK aide à trouver les transitions appropriées pour une spectroscopie Stark. Les moments dipolaires électriques permanents de la molécule polaire NaK sont déterminés expérimentalement pour deux états et les résultats sont comparés aux prédictions *ab initio*.

Mots-clés:

Spectroscopie Laser, calculs de chimie quantique, effet Stark

CONTENTS

Introduction	1
1. Diatomic molecules	5
1.1. Atomic units	6
1.2. The Hamiltonian for a diatomic molecule	7
1.3. Born-Oppenheimer approximation	10
2. Quantum chemistry calculations	13
2.1. Basic theory	14
2.1.1. Initial hamiltonian	14
2.1.2. Basis functions	15
2.1.3. Hartree-Fock procedure	17
2.1.4. Configuration interaction	19
2.2. The CIPSI package in Orsay	21
2.3. The sorting issue	22
2.4. An example: The Cs dimer	25
2.5. Determination of permanent electric dipole moments	28

3. Heatpipe study	33
3.1. Prerequisites	34
3.2. Heatpipe oven	34
3.3. Experimental setup for LIF detection	38
3.4. Analysis	39
3.5. Results	44
3.6. Cold Collisions	53
3.7. Potentials for beam experiments	55
4. Molecular beam setup	57
4.1. Chamber design	59
4.2. Molecular beam source	59
4.3. Optical system and photomultiplier	61
4.4. Rotational temperature of the potassium dimer	62
4.5. Velocity of the molecular beam	65
4.6. NaK - the first bandhead	66
4.7. Systematic exploration of the B state in NaK	67
4.8. A comment to the oven concept	70
5. Stark effect measurements	73
5.1. Stark shift formulas	74
5.2. Design of electrodes	76
5.3. Redesign of the lens system	78
5.4. The Stark effect of NaK experimentally	81
5.5. Evaluation of Stark spectra	83
5.6. Uncertainty budget	87
5.7. Results and comparison with <i>ab initio</i> data	88
6. Conclusion & Outlook	93
A. Transition frequencies B – X	101

B. Coherent dye lasers	111
B.1. Dye laser recipes	111
B.2. Adjustment of a Lyot filter	113
List of Figures	115
List of Tables	117
Bibliography	119
Curriculum Vitae	127
Publications	129

INTRODUCTION

Cooling and trapping of atoms has been done for some time now. With suitable transitions for cooling, alkalis, alkaline earth atoms and some special atoms are available as ultracold ¹ ensembles created and controlled by their inner and outer degrees of freedom [Wie99]. The interactions for most of these atomic gases however are quite simple at ultra low temperatures: spatially isotropic and sufficiently short range described effectively by contact potentials. In order to discover some interesting physics, it would be ideal to combine the regime of cold clouds of particles, where long interaction times are provided with long-range interactions that are anisotropic. The electric dipole-dipole interaction is an example for this [Stu05].

¹Collisions in a range from $1 \mu\text{K} \rightarrow 0$ are termed ultracold [Wei99]

In laboratories all over the world physicists have managed to cool down more than one species of atoms, and recently these overlapping atomic clouds have been transformed into clouds of heteronuclear molecules in their ground states (singlet and triplet) [Ni08].

Being composed out of two different sorts of atoms, these dimers yield a permanent electric dipole moment which determines the interaction between the particles and which can be studied in those experimental setups (at least for the ground state).

This thesis works in the same field, but approaches the interaction potentials and dipole moments from a different viewpoint. We do not start with clouds of atoms which are cooled and combined to form molecules, but create the molecules directly in a *hot* regime (room temperature or heated oven). The internal states are then manipulated with laser spectroscopy at molecular beam experiments, that provide very useful data for ultracold collision experiments.

Compared to a gas cell, a beam setup has the advantage to allow for Doppler free spectroscopy, therefore it is also called high resolution molecular spectroscopy. Only homonuclear molecules were investigated with beam experiments within this group before. Heatpipe measurements of heteronuclear dimers had been done with the disadvantage of Doppler broadening.

The task of this PhD thesis consists of several aspects:

1. Transfer the knowledge of high precision spectroscopy to the heteronuclear dimers and perform high resolution spectroscopy at a beam setup.
2. These molecules have new properties compared to homonuclear dimers (dipole moments). They should be explored with the new experiment in addition to conventional spectroscopy.

3. Calculate the size of the dipole moment with a theoretical approach beforehand to estimate the necessary precision and design the experiment

Chapters 1 and 2 will present the theoretical work that was done in Orsay in the framework of the *Cotutelle* agreement. The Hamiltonian of a diatomic molecule will be introduced together with the *Born-Oppenheimer Approximation* (BOA) being the underlying principle for physical models within this thesis. It will lead to the contents of Chapter 2, where the electronic part of the Hamiltonian is discussed in the scope of *ab initio* calculations.

The work on the code provides a better automation, efficiency, reliability and accuracy of the results. Among some improvements, that are described, this work yields a theoretical prediction of the permanent electric dipole moment function for the NaK dimer that is used afterwards to design an experiment for testing the calculation. This function shows a dependence on internuclear distance or vibrational quantum number for all electronic states.

Chapters 3, 4 and 5 will show the experimental part of the thesis (Hannover part of the *Cotutelle*). In order to build a high resolution beam setup it was necessary first to investigate the ground state(s) of NaK to improve their description (Chapter 3). An analysis of the spectra taken at the beam requires a precise knowledge of the electronic states involved. A joint description of singlet and triplet ground states is given with the help of the heat-pipe data and predictions of scattering length will be confirmed by the findings.

Chapter 4 describes the build-up of the vacuum chamber for the molecular beam and its characterization by a series of experiments. Excitation spectroscopy of the NaK B $^1\Pi$ - X $^1\Sigma^+$ covering the vibrational levels $v^* = 1 \dots 15$ results in assigned line positions and provides a basis for the search of suitable transitions for a

Stark spectroscopy.

Finally the dipole moments for both states ($X^1\Sigma^+$ and $B^1\Pi$) are measured. Chapter 5 illustrates the planning and modifications of the beam chamber for the Stark measurements. Transitions on three different vibrational bands of the excited state were recorded and evaluated carefully. At the end a comparison with the prediction calculated in Chapter 2 allows to compare the vibrational dependence.

DIATOMIC MOLECULES

Premise for all the description of diatomic molecules within this thesis is an approximation called the Born-Oppenheimer approximation (BOA). Its physical justification lies in the fact that electrons are light and move very fast compared to the nuclear motion. Therefore they can adapt instantaneously to any internuclear distance. This argument will lead to a separation ansatz for the wave functions under consideration and is stressed here, because this separation will directly connect to [Chapter 2](#) about quantum chemistry calculations.

1.1. Atomic units

Although every physical quantity has a unit in which it is measured, and all spectroscopic studies use a common set of these units, it is of advantage to carry out calculations in so called atomic units (a.u.) like proposed already in 1959 [Shu59]. Loosely spoken: in atomic units the quantities e (electron charge), m_e (electron mass) and \hbar (reduced Planck constant) have the value 1. All lengths or distances are then given in units of Bohr radii:

$$1 \text{ bohr} = a_0 = \frac{\hbar^2}{m_e e^2}, \quad (1.1)$$

and the atomic energy unit is:

$$1 \text{ hartree} = E_h = \frac{e^2}{a_0} = \frac{m_e e^4}{\hbar^2}. \quad (1.2)$$

To deduce units for the above quantities using the formulae given, one has to take the cgs-units of e , m_e and \hbar . In SI-units an additional factor of $4\pi\epsilon_0$ in Eq. (1.1) and $(4\pi\epsilon_0)^2$ in the denominator of Eq. (1.2) have to be applied. See Table 1.1 for details and for conversion recipes into atomic units. Table 1.2 lists some values for typical quantities used within this thesis.

In order to use the results of theoretical calculations for comparison with measured values one always has to convert the numbers given in a.u. using the most up to date experimental values of e , m_e and \hbar . The calculation itself is independent of these values and stays valid even when new measurements may bring new, more accurate values for these natural constants at a later time.

Another advantage of atomic units is, that all equations take a much simpler form. For example the Hamiltonian of the electron around the hydrogen nucleus has in SI units the following look:

$$\hat{\mathcal{H}} = -\frac{\hbar^2}{2m_e} \nabla^2 - \frac{1}{4\pi\epsilon_0} \frac{e^2}{r}$$

Quantity	Name	cgs-unit	SI-unit
Mass	Electron mass	m_e	m_e
Angular momentum	Reduced Planck constant, \hbar	\hbar	\hbar
Charge	Elementary charge	e	e
Length	Bohr, a_0	$\hbar^2/m_e e^2$	$4\pi\epsilon_0\hbar^2/m_e e^2$
Energy	hartree, E_h	e^2/a_0	$e^2/4\pi\epsilon_0 a_0$
Time		\hbar/E_h	\hbar/E_h
Frequency		E_h/\hbar	E_h/\hbar
Dipole moment		ea_0	ea_0
Momentum		\hbar/a_0	\hbar/a_0
Force		E_h/a_0	E_h/a_0
Current		eE_h/\hbar	eE_h/\hbar

Table 1.1.: Atomic units: the natural measure, in which physical quantities are expressed. Right columns: expressions in cgs- and SI-system

(assuming an infinite mass of the nucleus), while atomic units transform the preceding equation into

$$\hat{\mathcal{H}} = -\frac{1}{2}\nabla^2 - \frac{1}{r}.$$

For these reasons all equations given in the theoretical sections (Chapters 1 and 2) will be written in atomic units if not stated otherwise.

1.2. The Hamiltonian for a diatomic molecule

The Schrödinger equation for a diatomic molecule with a Hamiltonian acting on a wave function that accounts for motion of nuclei and electrons reads like this (molecular frame):

$$\hat{\mathcal{H}}\psi_{ne}(\mathbf{R}_n, \mathbf{r}_e) = E_{ne}\psi_{ne}(\mathbf{R}_n, \mathbf{r}_e), \quad (1.3)$$

Quantity	Atomic unit	Value
Length	1 a.u. = 1 bohr	0.052917720859 nm
Energy	1 a.u. = 1 hartree	4.35974394 10^{-18} J
	1 a.u. = 1 hartree	219474.6314 cm^{-1}
Dipole moment	1 a.u.	2.5417469 D

Table 1.2.: Unit-representation of typical quantities. Note that the dipole moment is given in Debye (D), which is in SI units: 1 D = 3.33564 10^{-30} C m. All numbers were derived using the constants from *2006 CODATA recommended values* [COD06].

where the indices ‘ ne ’ denote, that energy contributions from nuclear and electron motion are included. \mathbf{R}_n denotes the coordinates of the two nuclei in the molecule fixed coordinate system and \mathbf{r}_e the coordinates of all electrons respectively. The Hamiltonian \mathcal{H} has the following structure:

$$\hat{\mathcal{H}} = \hat{\mathcal{T}}_n + \hat{\mathcal{T}}_e + V(\mathbf{R}_n, \mathbf{r}_e), \quad (1.4)$$

where $\hat{\mathcal{T}}_n$ is the kinetic energy operator of the nuclei

$$\hat{\mathcal{T}}_n = - \sum_{\alpha=1}^2 \frac{1}{2M_\alpha} \nabla_{\mathbf{R}_\alpha}^2, \quad (1.5)$$

in cartesian coordinates:

$$\hat{\mathcal{T}}_n = - \sum_{\alpha=1}^2 \frac{1}{2M_\alpha} \left[\frac{\partial^2}{\partial X_\alpha^2} + \frac{\partial^2}{\partial Y_\alpha^2} + \frac{\partial^2}{\partial Z_\alpha^2} \right]. \quad (1.6)$$

Similarly one can write for the electrons:

$$\hat{\mathcal{T}}_e = -\frac{1}{2} \sum_i \nabla_{\mathbf{r}_i}^2 = -\frac{1}{2} \sum_i \left[\frac{\partial^2}{\partial x_i^2} + \frac{\partial^2}{\partial y_i^2} + \frac{\partial^2}{\partial z_i^2} \right]. \quad (1.7)$$

(Note that the electron mass does not appear here due to atomic units.) The potential energy term $V(\mathbf{R}_n, \mathbf{r}_e)$ contains Coulomb attraction between electrons and nuclei as well as Coulomb repulsion terms for interacting particles with same sign of charge (e - e, n - n):

$$\begin{aligned}
 V(\mathbf{R}_n, \mathbf{r}_e) = & - \sum_{\alpha} \sum_i \frac{Z_{\alpha}}{|\mathbf{R}_{\alpha} - \mathbf{r}_i|} + \sum_i \sum_{j>i} \frac{1}{|\mathbf{r}_i - \mathbf{r}_j|} \\
 & + \sum_{\alpha} \sum_{\beta>\alpha} \frac{Z_{\alpha} Z_{\beta}}{|\mathbf{R}_{\alpha} - \mathbf{R}_{\beta}|} \quad (1.8)
 \end{aligned}$$

In some publications for diatomic molecules ([Pas00] and [LB04]) one often finds also the following form of the total Hamiltonian:

$$\hat{\mathcal{H}} = \hat{\mathcal{T}}_n(R) + H^{ROT}(R, \Theta, \Phi) + \hat{\mathcal{T}}_e(\mathbf{r}_e) + V(R, \mathbf{r}_e) + H^{rel} \quad (1.9)$$

where the nuclear kinetic energy is split into two contributions. Here the nuclear coordinates are described by angles being more suited to handle rotation. In the same time a change of coordinate system has taken place, because rotation is only visible in the lab frame, while it does not exist in the molecular frame, apart through frame transformation from the lab frame. H^{rel} includes spin coordinates of the electrons. This description is mainly used by experimentalists who want to evaluate their spectra and have to deal with vibration and rotation. In quantum chemistry calculations (at least) for diatomics a cartesian coordinate system is used. Spin coordinates are here introduced by build-up of product functions (see Chapter 2).

1.3. Born-Oppenheimer approximation

In the BOA as a first step the wave function $\psi_{ne}(\mathbf{R}_n, \mathbf{r}_e)$ is factorized

$$\psi_{ne}(\mathbf{R}_n, \mathbf{r}_e) = \psi_n(\mathbf{R}_n)\psi_e(\mathbf{R}_n, \mathbf{r}_e), \quad (1.10)$$

where the wave function of rotation and vibration, $\psi_n(\mathbf{R}_n)$, only depends on the coordinates of the nuclei, while the wave function for the electron motion, $\psi_e(\mathbf{R}_n, \mathbf{r}_e)$ depends on the coordinates of nuclei and electrons. The latter wave function is the solution of the so called *electronic Schrödinger equation*:

$$[\hat{\mathcal{T}}_e + V(\mathbf{R}_n^{(0)}, \mathbf{r}_e)]\psi_e(\mathbf{R}_n^{(0)}, \mathbf{r}_e) = V_e(\mathbf{R}_n^{(0)})\psi_e(\mathbf{R}_n^{(0)}, \mathbf{r}_e) \quad (1.11)$$

that is solved for fixed coordinates of the nuclei $\mathbf{R}_n = \mathbf{R}_n^{(0)}$. The eigenvalues $V_e(\mathbf{R}_n^{(0)})$ will then depend parametrically on the nuclear coordinates. The resulting eigenvalue as function of $\mathbf{R}_n^{(0)}$ is called Born-Oppenheimer potential function. Traditional quantum chemistry calculations are concerned only with solving (1.11). Rotational and vibrational eigenstates are not considered. Chapter 2 will describe the details of this kind of calculation. Merging the product ansatz (1.10) and (1.11) in Eq. (1.3) gives:

$$[\hat{\mathcal{T}}_n + V_e(\mathbf{R}_n)]\psi_n(\mathbf{R}_n)\psi_e(\mathbf{R}_n, \mathbf{r}_e) = E_{ne}\psi_n(\mathbf{R}_n)\psi_e(\mathbf{R}_n, \mathbf{r}_e) \quad (1.12)$$

Up to now it was only assumed that we can write the eigenstate as a product of electronic and nuclear wave functions. We now introduce the second step of the BOA into Eq. (1.12):

$$\hat{\mathcal{T}}_n[\psi_n(\mathbf{R}_n)\psi_e(\mathbf{R}_n, \mathbf{r}_e)] = \psi_e(\mathbf{R}_n, \mathbf{r}_e)[\hat{\mathcal{T}}_n\psi_n(\mathbf{R}_n)] \quad (1.13)$$

The effect of the differential operator $\hat{\mathcal{T}}_n$ on the electronic wave function $\psi_e(\mathbf{R}_n, \mathbf{r}_e)$ is neglected. This is the Born-Oppenheimer

approximation. When we rewrite (1.12) with the approximation of (1.13), the following simplified Schrödinger equation evolves:

$$[\hat{T}_n + V_e(\mathbf{R}_n)]\psi_n(\mathbf{R}_n) = E_{ne}\psi_n(\mathbf{R}_n) \quad (1.14)$$

It does not contain any electron coordinates any more and describes formally the motion of N nuclei in the potential $V_e(\mathbf{R}_n)$. The eigenvalues E_{ne} of this equation are total energies with contributions of nuclear and electron motion. By the Born-Oppenheimer approximation the effect of electronic motion is solely described by the potential function $V_e(\mathbf{R}_n)$. The physical interpretation of this approximation was given already at the beginning of this chapter: the electrons are much faster than the nuclei, so from the point of view of the former the nuclei are immobile. It is justified to assume that the electronic energy is only depending on the position of the nuclei, not on their velocities. For every nuclear geometry \mathbf{R}_n a *quasi-stationary* electronic state emerges that is defined by the wave function $\psi_e(\mathbf{R}_n, \mathbf{r}_e)$. The situation described by this wave function are the fixed nuclei in geometry \mathbf{R}_n and the electrons that move in the Coulomb field of the fixed nuclei (and in the Coulomb field of the other electrons of course). The contribution of the electrons to the total energy in this approximation is the energy of the quasi-stationary state, which is $V_e(\mathbf{R}_n)$.

QUANTUM CHEMISTRY CALCULATIONS

This chapter will present the main ideas of a quantum chemistry configuration interaction (CI) calculation for diatomic molecules done by the `AUTOCHIP` routine developed in the group of Olivier Dulieu in Orsay. It is making use of a set of `FORTRAN 77` programs that implement the *CIPSI* procedure [Hur73, Eva83].

The fully functional code had some drawbacks that were addressed within the scope of this thesis. With a new sorting algorithm (Sec. 2.3) automation and efficiency were improved. Recently the accuracy at large internuclear distances was also enhanced (Sec. 2.4).

Calculations were performed for several heteronuclear dimers namely: LiCs, LiRb, LiK, NaK, RbCs, KCs and for three homonuclear dimers: Cs₂, Rb₂ and H₂. Using the examples of Rb₂, Cs₂ and NaK some of the improvements and results will be shown.

2.1. Basic theory

The following description will use atomic units throughout the whole chapter about CI calculations. In these branches of physics everything is done in atomic units, which makes the results to obtain independent of any physical constant, i.e. more universal (see Sec. 1.1).

A more detailed elaboration on methods of quantum chemistry and configuration interaction calculations can be found in [Jen97, Sza96].

To actually perform a calculation one has to choose a core geometry, which means for a diatomic molecule to choose an internuclear distance. It only has six cartesian coordinates for the cores $(X_1^{(0)}, Y_1^{(0)}, Z_1^{(0)}, X_2^{(0)}, Y_2^{(0)}, Z_2^{(0)})$ but the electronic energy only depends on the parameter R :

$$R = \sqrt{\left(X_1^{(0)} - X_2^{(0)}\right)^2 + \left(Y_1^{(0)} - Y_2^{(0)}\right)^2 + \left(Z_1^{(0)} - Z_2^{(0)}\right)^2} \quad (2.1)$$

To determine the complete function $V_e(R)$ in Eq. (1.11) one has to repeat the *ab initio* calculation of the electronic Schrödinger equation at different internuclear distances R .

2.1.1. Initial hamiltonian

We start with the Hamiltonian of the *electronic Schrödinger equation* (1.11) and write down all terms explicitly in the molecular frame, neglecting interaction with spins (Eqs. (1.7) and (1.8)):

$$\hat{\mathcal{H}}_e = -\frac{1}{2} \sum_i \nabla_{\mathbf{r}_i}^2 - \sum_\alpha \sum_i \frac{Z_\alpha}{|\mathbf{R}_\alpha - \mathbf{r}_i|} + \sum_i \sum_{j>i} \frac{1}{|\mathbf{r}_i - \mathbf{r}_j|} \quad (2.2)$$

The term of nuclear repulsion (compare Eq. (1.8)) is a constant for a given core geometry or internuclear distance, which is only a

parameter in the calculation. We can therefore neglect it for the time being and add it at a later time for the calculation of the nuclear motion or the total charge distribution. The remaining terms can be grouped into two contributions:

$$\begin{aligned} \mathcal{H}_e &= \sum_i \underbrace{\left(-\frac{1}{2} \sum_i \nabla_{\mathbf{r}_i}^2 - \sum_{\alpha} \frac{Z_{\alpha}}{|\mathbf{R}_{\alpha} - \mathbf{r}_i|} \right)}_{\hat{h}(\mathbf{r}_i, \mathbf{p}_i)} + \sum_{j>i} \underbrace{\sum_i \frac{1}{|\mathbf{r}_i - \mathbf{r}_j|}}_{\hat{g}(\mathbf{r}_i, \mathbf{r}_j)} \\ &= \sum_i \hat{h}(\mathbf{r}_i, \mathbf{p}_i) + \sum_{j>i} \hat{g}(\mathbf{r}_i, \mathbf{r}_j) \quad (2.3) \end{aligned}$$

where $\hat{h}(\mathbf{r}_i, \mathbf{p}_i)$ and $\hat{g}(\mathbf{r}_i, \mathbf{r}_j)$ are the so called one- and two-electron-operators respectively, depending on the number of electrons they work on.

$$\mathbf{r}_i = (x_i, y_i, z_i) \quad \text{and} \quad \mathbf{p}_i = \left(-i \frac{\partial}{\partial x_i}, -i \frac{\partial}{\partial y_i}, -i \frac{\partial}{\partial z_i} \right) \quad (2.4)$$

($i = 1, 2, \dots, n$) are the current space coordinates and momenta of the i^{th} electron in the molecule fixed coordinate system.

2.1.2. Basis functions

Solving the Schroedinger equation starts out with choosing a set of (atomic) basis functions to construct the molecular orbitals via *Linear combination of atomic orbitals* (LCAO) :

$$\chi_j(\mathbf{r}_i) = \sum_{\mu=1}^{N_{orb}} c_{\mu j} \phi_{\mu}(\mathbf{r}_i) \quad (2.5)$$

The set of basis functions $\phi_{\mu}(\mathbf{r}_i)$ can be any complete set of (orthogonal) functions (from which only a limited number N_{orb} are

$$\begin{aligned}
g_s(\alpha, \mathbf{r}) &= \left(\frac{2\alpha}{\pi}\right)^{\frac{3}{4}} \exp(-\alpha r^2) & g_{p_z}(\alpha, \mathbf{r}) &= \left(\frac{128\alpha^5}{\pi^3}\right)^{\frac{1}{4}} z \exp(-\alpha r^2) \\
g_{p_x}(\alpha, \mathbf{r}) &= \left(\frac{128\alpha^5}{\pi^3}\right)^{\frac{1}{4}} x \exp(-\alpha r^2) & g_{d_{xx}}(\alpha, \mathbf{r}) &= \left(\frac{2048\alpha^7}{9\pi^3}\right)^{\frac{1}{4}} x^2 \exp(-\alpha r^2) \\
g_{p_y}(\alpha, \mathbf{r}) &= \left(\frac{128\alpha^5}{\pi^3}\right)^{\frac{1}{4}} y \exp(-\alpha r^2) & g_{d_{xy}}(\alpha, \mathbf{r}) &= \left(\frac{2048\alpha^7}{\pi^3}\right)^{\frac{1}{4}} xy \exp(-\alpha r^2)
\end{aligned}$$

Table 2.1.: The low order GTOs. The orbital for $l = m = n = 0$ is called s-orbital, because it is the simplest orbital with spherical symmetry. The sum $p + m + n = 1$ is then called p orbital, $p + m + n = 2$ d orbital, ... (compare Eq. (2.6) to the expressions above)

taken). The most obvious choice would be hydrogen-like *Slater orbitals* (STO) [Sla30], but Gaussian basis sets (GTO)

$$g(\alpha, \mathbf{r}) = g(\alpha, l, m, n; x, y, z) = N e^{-\alpha r^2} x^l y^m z^n \quad (2.6)$$

have the advantage to speed up calculations, because integrals for the one- and two-electron-operators [Sza96] can be solved analytically with Gaussian functions [Bro96] (l, m, n , are here only positive integers, no quantum numbers). Table 2.1 gives examples for the first few GTOs.

The electron spin is considered by building product functions with the spin functions $|s, m_s\rangle$: $\alpha(\xi) = |\frac{1}{2}, \frac{1}{2}\rangle$ and $\beta(\xi) = |\frac{1}{2}, -\frac{1}{2}\rangle$, with the spin coordinate ξ . The resulting *spin orbitals* are:

$$\psi_{j,\alpha}(\mathbf{r}_i, \xi_i) = \chi_j(\mathbf{r}_i)\alpha(\xi_i) \quad \text{or} \quad \psi_{j,\beta}(\mathbf{r}_i, \xi_i) = \chi_j(\mathbf{r}_i)\beta(\xi_i) \quad (2.7)$$

With every $\chi_j(\mathbf{r}_i)$ we can construct two spin orbitals, so that every spatial wave function can be used twice without violating the *Pauli principle*.

2.1.3. Hartree-Fock procedure

Every quantum chemistry calculation aims to solve the *electronic Schrödinger equation* (1.11) for a system of n electrons with the Hamiltonian written in the form of one- and two-electron operators (2.3):

$$\begin{aligned} \mathcal{H}_e \psi_e(\mathbf{r}_1, \mathbf{r}_2, \dots, \mathbf{r}_n) &= \left[\sum_{i=1}^n \hat{h}(\mathbf{r}_i, \mathbf{p}_i) + \sum_{j>i} \hat{g}(\mathbf{r}_i, \mathbf{r}_j) \right] \psi_e(\mathbf{r}_1, \mathbf{r}_2, \dots, \mathbf{r}_n) \\ &= E_e \psi_e(\mathbf{r}_1, \mathbf{r}_2, \dots, \mathbf{r}_n) \quad (2.8) \end{aligned}$$

The most general way to construct a n -electron wave function is to construct a *Slater determinant* out of the spin orbitals (2.7):

$$\begin{aligned} \Psi_e(\mathbf{r}_1, \xi_1, \mathbf{r}_2, \xi_2, \dots, \mathbf{r}_n, \xi_n) &= \frac{1}{\sqrt{n!}} \begin{vmatrix} \psi_1(\mathbf{r}_1, \xi_1) & \psi_2(\mathbf{r}_1, \xi_1) & \psi_3(\mathbf{r}_1, \xi_1) & \dots & \psi_m(\mathbf{r}_1, \xi_1) \\ \psi_1(\mathbf{r}_2, \xi_2) & \psi_2(\mathbf{r}_2, \xi_2) & \psi_3(\mathbf{r}_2, \xi_2) & \dots & \psi_m(\mathbf{r}_2, \xi_2) \\ \vdots & \vdots & \vdots & \vdots & \vdots \\ \psi_1(\mathbf{r}_n, \xi_n) & \psi_2(\mathbf{r}_n, \xi_n) & \psi_3(\mathbf{r}_n, \xi_n) & \dots & \psi_m(\mathbf{r}_n, \xi_n) \end{vmatrix} \\ & \quad (2.9) \end{aligned}$$

This ensures that the total wave function does have the correct symmetry properties when exchanging two electrons, i.e. the *Pauli principle* is automatically fulfilled. The equation above is valid for an even number of electrons $n = 2m$ (closed shells). The electrons are distributed in $n/2 = m$ spatial functions. Usually

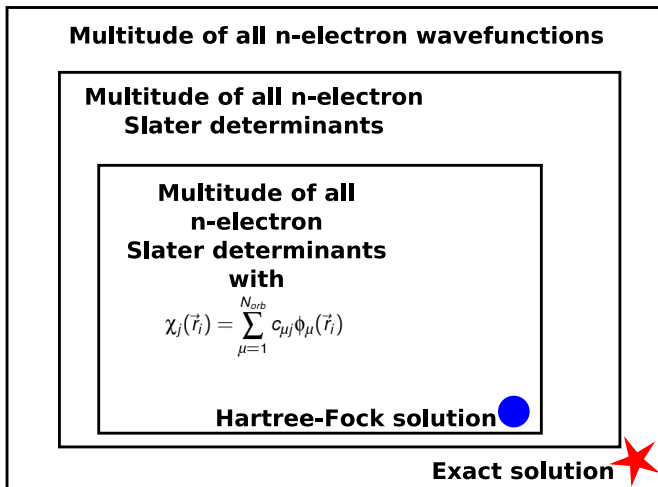


Figure 2.1.: Graphical representation of the space of n-electron wave functions. Slater determinants with fixed N_{orb} , which can be expressed as a linear combination of atomic orbitals are represented by the most inner rectangle. By varying the coefficients $c_{\mu j}$ one can move around the parameter space.

N_{orb} in Eq. (2.5) is chosen to be $N_{orb} \gg m$. For generalization of the Slater determinant to cases of non-closed shells see [Jen97]. The *Hartree-Fock procedure* minimizes now the Energy E_e in (2.8) for a given internuclear distance using a variational calculus. The variation is done by changing the coefficients $c_{\mu j}$ in the spatial part $\chi_j(\mathbf{r}_i)$ of the spin orbitals (2.5).

Fig. 2.1 shows a graphical representation of the procedure: variation of coefficients $c_{\mu j}$ implies that one is moving around the most inner rectangle, which is the multitude of all n-electron Slater determinants, that consist of functions of the form (2.5) with N_{orb} basis functions. This is only a subset of all possible

n-electron Slater determinants. The best set of $c_{\mu j}$ is represented by the circle in the lower right corner. It is most near to the exact solution which is the star in the figure. By increasing the number of orbitals N_{orb} in (2.5), which just means to use more basis functions, one can get a better approximation of the exact solution, because for $N_{orb} \rightarrow \infty$ the two inner rectangles would merge and the circle could come closer to the exact solution. Nevertheless it can be shown that the exact solution can never be expressed by a *single* Slater determinant, because electron correlation is not modelled correctly [Jen97].

2.1.4. Configuration interaction

Usually the number of orbitals N_{orb} is much higher than the number of electrons which have to be treated in the procedure. After *filling* the electrons into the orbitals, some will remain unoccupied. These additional spatial functions are also called *virtual orbitals*, which give rise to two times the number of *virtual spin orbitals*. A certain Slater determinant with a given set of spin orbitals, where some of them are filled with electrons, and the rest are virtual is often called a *configuration*. Such a configuration Ψ_0^{HF} is a typical outcome of a Hartree-Fock calculation, which has to precede every *configuration interaction* calculation. Within a given Slater determinant

$$\Psi_0^{HF} = \Psi_0^{HF}(\psi_1, \psi_2, \dots, \psi_a, \psi_b, \dots, \psi_m) \quad (2.10)$$

one can substitute now an occupied orbital ψ_a by a virtual one (ψ_r), and thereby promote an electron to a formerly virtual orbital. This process is called *single excitation* and the result a *singly excited determinant* $\Psi_a^r(\psi_1, \psi_2, \dots, \psi_r, \psi_b, \dots, \psi_m)$. *Double excitation*: $\Psi_{ab}^{rs} = \Psi(\psi_1, \psi_2, \dots, \psi_r, \psi_s, \dots, \psi_m)$ is introduced

in the same way. The main idea behind configuration interaction is now to not just take a single Slater determinant to solve the Schrödinger equation (2.8), but to take the best approximation, which comes out of an Hartree-Fock calculation and construct a new wave function which is a linear combination of the zero-order Hartree-Fock solution and of substituted determinants (single, double, ...):

$$\Psi_0^{(CI)} = a_{00}\Psi_0^{(HF)} + \sum_{s>0} a_{s0}\Psi_s^{(HF)} \quad (2.11)$$

The coefficients a_{xy} in this ansatz for the wave function give now the degree of freedom to get closer to the exact solution of the electronic problem, which means approaching the star in Fig 2.1.

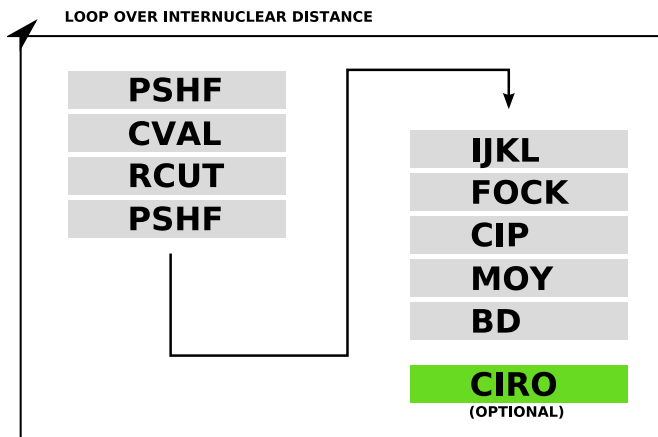


Figure 2.2.: AUTOCIP: Automatic calling of subroutines and processing their output into R-dependent potential energy curves, dipole moments or spin-orbit matrix elements

2.2. The CIPSI package in Orsay

The AUTOCIP routine calls a chain of sub-programs, which are described below. Their names display the steps of the *ab initio* procedure described in the last section. A specific feature of these calculations is the use of effective core potentials (ECP) [Dur74, Dur75, Fou92]. The alkali pair is described as an effective two electron system, where the electrons move in a field of two polarizable cores. To describe the dynamic core-polarization in a correct manner, a cutoff function [Mue84, Fou92] is necessary to ensure correct physical behaviour when an electron enters a core. One cutoff radius is introduced for each atom. It corresponds to the *size* of the ionic core (the cutoff functions have spherical symmetry). By adjusting this parameter the ground state ionization energy of the atom can be correctly set.

With one single parameter, it is possible to tune exactly one atomic level or to approximate a number of atomic levels as a compromise. To overcome this limitation one can introduce ℓ -dependent cutoff functions into the core polarization potential [Fou92] with more than one adjustable parameter. This allows to adjust e.g. the s-, p- and d-energy levels of the molecular fragments ($\ell = 0, 1, 2$). The tasks of the routines in detail are:

PSHF calculates RHF- or UHF-SCF¹ molecular wave functions and allows for usage of pseudo-potentials. The atomic cores are described by the pseudo-potentials of Durand and Barthelat [Dur74, Dur75]. The second call (see Fig. 2.2) is needed to get the polarized molecular orbitals.

¹RHF calculations are *restricted* to an even number of electrons, while UHF means *unrestricted* [Jen97]. SCF: *Self consistent field* calculation is another name for Hartree-Fock calculations.

CVAL takes care of polarization effects. Core polarization is taken into account through a ℓ -dependent effective core potential (ECP) depending on the dipole polarizabilities $\alpha_d^{M^+}$ and $\alpha_d^{M'^+}$ of the M^+ and M'^+ ions [Aym05],

RCUT includes the of ℓ -dependent cutoff parameters ρ_ℓ , adjusted to reproduce the experimental energies of the two lowest s , p , and d atomic levels.

IJKL calculates overlap integrals and two electron integrals for the CI. On HF-level PSHF is doing this calculation itself.

FOCK builds density matrix and Fock operator $F_{\mu\nu}$ [Jen97].

CIP sets up linear combinations of Slater determinants (first part of the full valence CI).

MOY is a matrix construction program.

BD performs diagonalization of matrices.

CIRO calculates density matrix for states and transitions, and finally permanent and transition dipole moments [Dur92].

2.3. The sorting issue

The subroutines described in the last section write down the wave vectors and eigenenergies into text files that are read out by the AUTOCIP program. Unfortunately in the process of calling the subroutines and later reading their output files the program loses track of the correct order of singlet and triplet states. In order to regain this information and then search for the proper eigenenergies, which are stored at a different position in the output files, some empirical method was used in the past to decide, if a vector

has singlet or triplet character. Symmetric and anti-symmetric components were counted to determine the symmetry.

Calculations are done on a fine grid in internuclear distance space (as computers can do today) and the sorting of states should be as automatic as possible, because the amount of numbers generated by the code is huge. Human intervention and error correction takes a lot of time and effort and is not fail-safe.

A result of the old sorting method can be seen in Fig. 2.3 (a): due to a wrong decision of the routine jumps appear at $R = 28$ a.u. in all $^1\Sigma_g^+$ states of Rb_2 . The reason is that singlet or triplet character gets lost at big internuclear distances. The first state (ground state) is not recognized as a $^1\Sigma_g^+$ state and the corresponding eigenenergy is calculated, but thrown away by the sorting algorithm. As a result all asymptotes jump to the next state of same symmetry. The behaviour can be observed for other symmetries as well.

A new method was implemented to solve this problem. It uses a very fundamental principle of quantum mechanics: eigenvectors of a given symmetry do not change too much from a given internuclear distance to the next one, and that the product of the states belonging to the same symmetry should be equal or near to one, whereas the product between states of different symmetry should be (more or less) zero, because states of every quantum mechanical system form an orthogonal basis set (or are constructed like this using GTOs).

A routine for *comparison of eigenvectors* (by building the scalar product) was implemented into the existing code, and indeed it helped sorting the states (Fig 2.3 (b)). The drawback with this method is of course, that one has to set the symmetries once or determine them with a different method (like the old sorting), and then remember the symmetries of the last internuclear distance.

To overcome this weakness, a third method was implemented

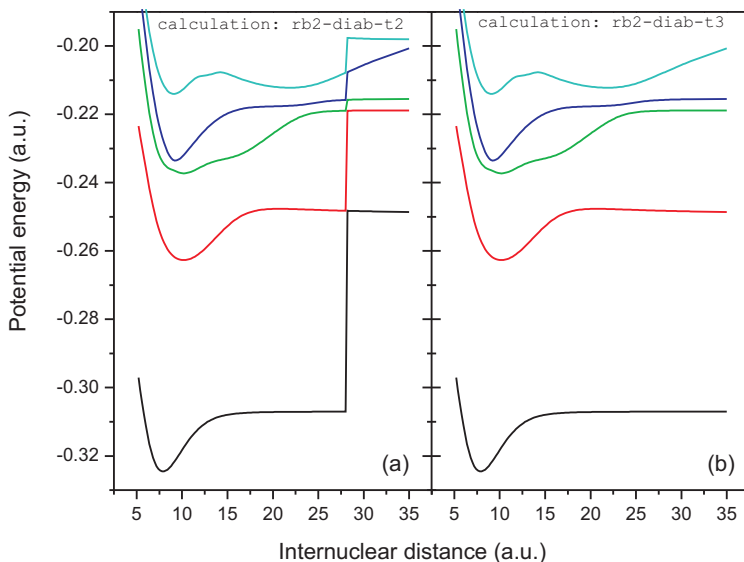


Figure 2.3.: Calculation of the first five ${}^1\Sigma_g^+$ states of Rb_2 sorted (a) with looking pairwise at final wave function components for each internuclear distance R and (b) with evaluating scalar products of vector for R with vector from internuclear distance one step before.

recently, that counts for single or double excitations (see Subsection 2.1.4) and saves the information which vector has which symmetry. Hereby a sorting is not necessary any more after the calculation. In the search for the eigenvector of the state under consideration, one just has to look up an unique identification number that was saved with this vector and find out, if this vector contains any single or double excitations. By this the symmetry is determined. This type of sorting was tested in a recent calcu-

lation on Cs₂ (see next section), but has not proven to be fully reliable (there are still jumps observed in the asymptotic region). Sorting for Cs₂ (next section) was done with the method of vector comparison.

2.4. An example: The Cs dimer

The use of more than one cutoff radius in the RCUT routine [Fou92] gives the possibility to adjust the energies of atomic levels to experimental values. Unfortunately the potential energy curves of the dimer will show residual $1/R^4$ behaviour in the long range part of the curve, which is a purely analytical issue connected with the choice of the ℓ -dependent ECP. When a molecule dissociates into two neutral fragments, the core polarization potential (CPP) must vanish. And this is achieved via mutual cancellation of the electron-other core and the core-core interaction terms at large internuclear distances. A ℓ -dependent choice of cutoff functions does not ensure this vanishing [Gue09].

The simpler approach of using only one cutoff radius (subroutine RPOL instead of RCUT in program chain) in the core polarization potential exhibits the right long range behaviour, but does not allow for adjusting all asymptotic energies correctly. Usually only the ground state energy is set [Mue84].

In order to use more than one cutoff parameter and still have the right behaviour in the long range part of the potential energy curves a calculation for Cs₂ was set up, which uses the ℓ -independent approach and fixes the Cs(6s) energy to the experimental value, and then adds the ℓ -dependent term as a small correction to the former in order to bring the Cs(6p) and Cs(5d) energies to their experimental values without changing the Cs(6s) energy. The exact form of the CPP can be found in [Gue09].

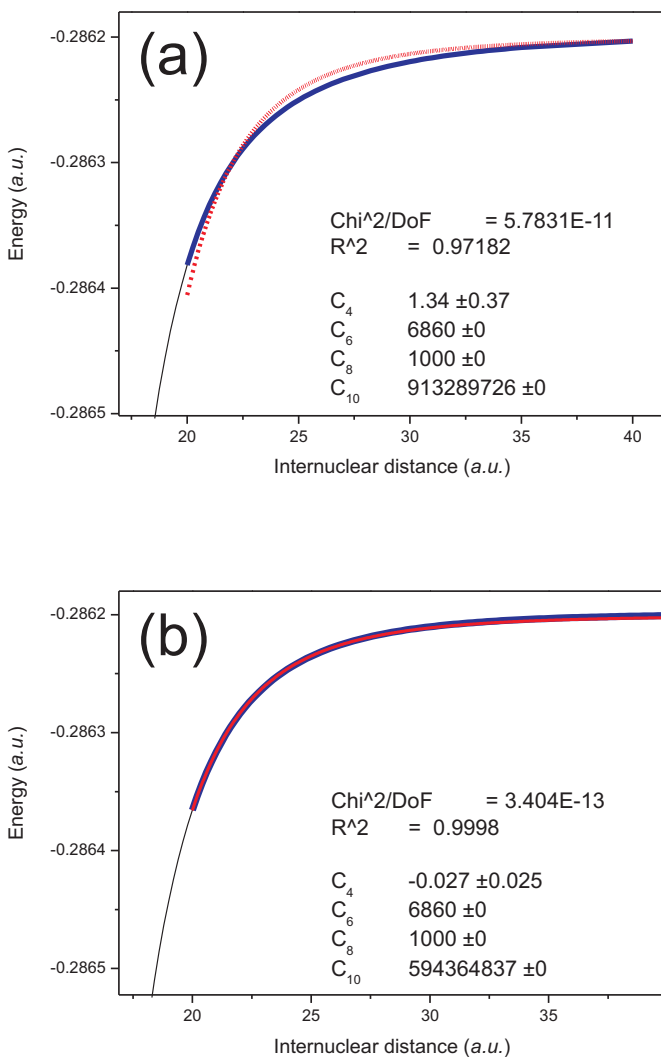


Figure 2.4.: Comparison of C_4 fit of the current implementation (b) to the result of former calculations, before 05/2009 (a). Thin lines are the potential energy curves, dashed the fit with $C_4 = 0$ and variation of C_{10} and solid the final step of variation of C_4 with C_{10} fixed.

A check was performed to assure that the $1/R^4$ behaviour of former calculations is really removed by this approach. Therefore an older Cs_2 calculation (a) was compared to the new setup (b). In Fig. 2.4 the long range parts for the Cs_2 ground state can be seen for both calculations. *Long range* is defined here by R values greater than the Le Roy radius [LeR74], which is $R_L = 20$ a.u. for Cs_2 [Ami02].

The function

$$V_{LR}(R) = D_e - \frac{C_4}{R^4} - \frac{C_6}{R^6} - \frac{C_8}{R^8} - \frac{C_{10}}{R^{10}} \quad (2.12)$$

was fitted to the ab initio points but not straightforward, because the C_n coefficients have shown to be highly correlated [Ger08]. The values $C_6 = 6860$ a.u. and $C_8 = 1000$ a.u. were taken from theoretical work [Kot00] and fixed in the fit. D_e was also fixed to $D_e = -0.28620078$ a.u.

With C_4 fixed to zero, the first step was to vary C_{10} . From the physical point of view the description with these three C_n parameters should be complete. For the new calculation (b) the agreement is already quite good, whereas the old calculation (a) shows deviations (this first step of fitting is shown in Figure 2.4 as dashed curves, for (b) is already overlapping with the dotted potential energy curve and the final fit).

In a second step the so found parameter C_{10} was kept fixed and C_4 was varied to check, if it is necessary to describe the *ab initio* curve (this second step of the fit is drawn as solid curves in Fig. 2.4). Table 2.2 shows final parameter sets. The description of the curve (a) requires an amount of C_4 , which is not necessary for (b) at all (for the new calculation (b) C_4 is of the same magnitude as the fitting error, so it could be set to zero). Furthermore the reduced χ^2 value after these steps is in (a) two magnitudes of order bigger than for (b). Clearly the dependence on C_4 is negligible

Fit parameters	(a)	(b)
C_4	1.3436	-0.0275
C_6	6860 •	6860 •
C_8	1000 •	1000 •
C_{10}	913[6]	594[6]
Reduced χ^2	5.78[-11]	3.40[-13]

Table 2.2.: Comparison of fit parameters. (a) and (b) are the fits with stepwise variation of C_4 and C_{10} . Numbers in brackets are powers of ten. Entries marked with • were fixed.

for the new calculation.

A publication of extensive sets of potential energy curves and transition dipole moments for Cs_2 , which has used this improved ECP, is in preparation [Aym09]. Unfortunately the procedure cannot be used for heteronuclear dimers, because some terms in the evaluation of the core polarization potential do not vanish in this case [Gue09].

It should be mentioned that all publications, that used CIPSI with effective ℓ -dependent potentials, had this underlying $1/R^4$ term, which was not noticed at the time of publishing.

2.5. Determination of permanent electric dipole moments

As pointed out before the *ab initio* calculation produces the complete set of eigenenergies *and* eigenvectors. With this information other physical properties of the system can be calculated easily.

The classical definition for the dipole moment is

$$\mu = \sum_{i=1}^N q_i \mathbf{r}_i \quad (2.13)$$

for a collection of N particles of charge q_i at position vectors \mathbf{r}_i . Note that its value depends on the coordinate system. The quantum mechanical expression for this quantity (for a molecule with N electrons and S nuclei) is given by:

$$\mu = \left\langle \Psi \left| - \sum_{\mu}^N \mathbf{r}_{\mu} \right| \Psi \right\rangle + \sum_k^S Q_k \mathbf{R}_k \quad (2.14)$$

where $q_{\mu} = -1$ for electrons and $q_k = Z_k$ for nuclei. \mathbf{R}_k is the position vector of the k th nucleus [Pil01]. For a diatomic molecule the expression reduces to

$$\mu = \left\langle \Psi \left| - \sum_{\mu}^N z_{\mu} \right| \Psi \right\rangle + \sum_{k=1}^2 Q_k z_k \quad (2.15)$$

due to cylinder symmetry. By a clever choice of the origin (i.e. the center of charge) the contributions of the nuclei cancel to zero. Otherwise they have to be included.

In AUTOCIP the calculation is activated by executing the program CIRD, which is called at the end of each run for each internuclear distance (Fig. 2.2).

Figure 2.5 shows the permanent electric dipole moment functions of the $(1)^1\Sigma^+$ state (X state, already published in [Aym05]) and $(1)^1\Pi$ state (B state) of NaK. A negative dipole moment reveals an electron transfer yielding a $\text{Na}^- \text{K}^+$ arrangement, while the positive dipole moment in the excited electronic state means that the electron is transferred towards the potassium atom.

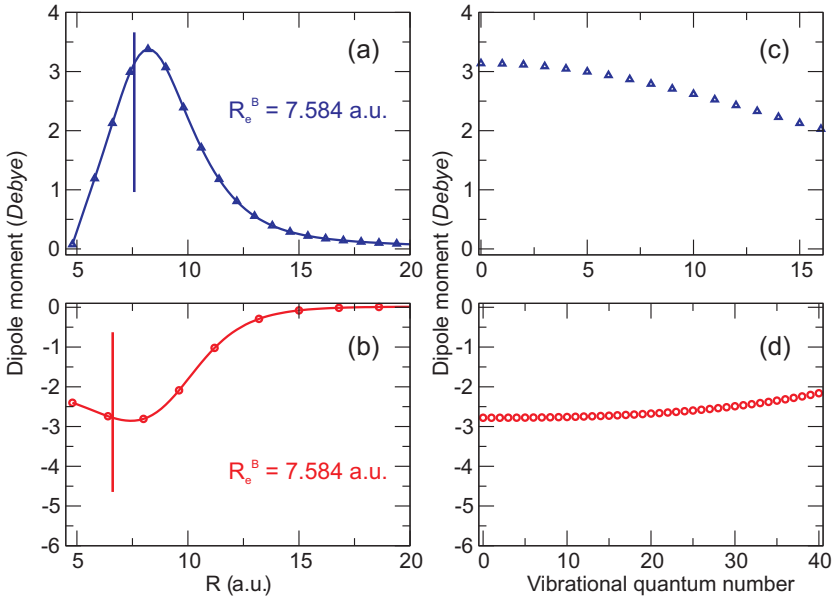


Figure 2.5.: Permanent electric dipole moments as a function of internuclear separation and of vibrational quantum number for the $X^1\Sigma^+$ state, (b) + (d), and the $B^1\Pi$ state, (a) + (c), of the NaK molecule. The vertical bars in (a) and (b) indicate the equilibrium internuclear distances R_e^B and R_e^X for $B^1\Pi$ state and $X^1\Sigma^+$ state respectively.

The variation of the dipole moment over internuclear distance is shown in parts (a) and (b) of the figure, while the dependence on the vibrational quantum number is shown in (c) and (d). The potentials used to calculate the vibrational dependence were not the *ab initio* curves but the experimental potentials given in [Ger08] and [Kat90]. For the ground state (d) the relative change from $v = 0$ to $v = 40$ is about 22%, for the excited state (c) the relative change from $v = 0$ to $v = 16$ is about 35%

The interest in those particular dipole moment functions for the NaK molecule is due to the experimental implementation of a beam apparatus, which will be introduced in Chapter 4. The curves in Fig. 2.5 display dipole moments of a few Debye typical for alkali dimers. As mentioned in the Introduction the molecular beam setup will allow to measure the v dependence of the permanent electric dipole moment. Taking the numbers from this *ab initio* prediction, one is able to estimate the size of the Stark effect, i.e. the splitting of molecular lines for a given electric field (Chapter 5.1).

The information from theory is thereby crucial to plan and design a high resolution experiment that applies electric fields big enough to observe the desired effect. The calculated v dependence also tells what accuracy one has to reach to determine it experimentally and thus to check the prediction.

HEATPIPE STUDY

Although NaK is one of the heteronuclear alkali diatomics which has been most frequently studied spectroscopically, a new analysis of the ground states for the singlet and triplet system was performed. Two strategies were followed: firstly, the range of observed levels of the triplet state was extended and secondly, a joint description of both potentials had to be found. This joint evaluation especially for the asymptotic part of the potential energy curves (PEC) as both electronic states share the same asymptote had not been done before for NaK. It should extend the reliability of predictions of cold collisions properties of Na with K. A good agreement with predictions was found (see Sec. 3.6).

In addition the molecular beam apparatus, that will be introduced in Chapter 4, required such a preliminary study. A comment on this can be found in Section 3.7.

3.1. Prerequisites

The electronic ground state, the $X^1\Sigma^+$ state, has been evaluated extensively with Fourier-transform spectroscopy by Russier-Antoine et al. in 2000 [RA00]. In contrast, the data for the triplet ground state are not that complete. First measurements by Bredford and Engelke [Bre79] were followed by a refinement of the description by Ross et al. [Ros85, Ros86], giving a RKR potential in [Ros85], and later by Ishikawa et al., providing an IPA potential [Ish94], where the RKR ansatz is corrected by an assumed perturbation, that is fitted to the experimental data (IPA = Inverted Perturbation Approach). Zemke and Stwalley [Zem99] reviewed the spectroscopic data available for both ground states building hybrid potentials for different regions of internuclear distance and determined long range dispersion terms and exchange energies. In 2000 Ferber et al. revisited low lying triplet states [Fer00] and were mainly concerned with the short range repulsive part of the PECs. Venturi et al. [Ven01] calculated singlet and triplet scattering lengths by constructing cubic spline interpolated potentials from the data in [RA00] and [Ish94] and pointed out, that precise spectroscopic measurements of the least bound rovibrational levels are needed in order to reduce uncertainties in the determination of the scattering length.

3.2. Heatpipe oven

The heatpipe is a stainless steel tube with a length of 880 mm and an outer diameter of 34 mm (wall thickness 2 mm) which is heated in the middle by a resistance heater ¹ and cooled at both ends with rings made of brass, where water flows through with

¹Carbolite: Model HST 12/-/400, Controller E102

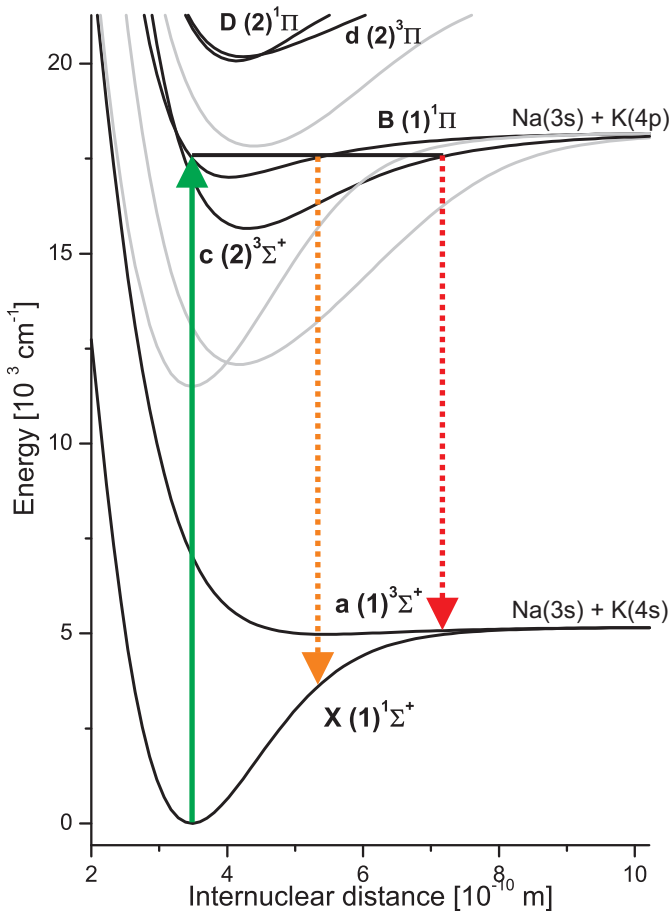


Figure 3.1.: Overview of potential energy curves according to the calculation in [Aym07]. The singlet and triplet ground electronic states and the excited states selected for the present measurement are highlighted.

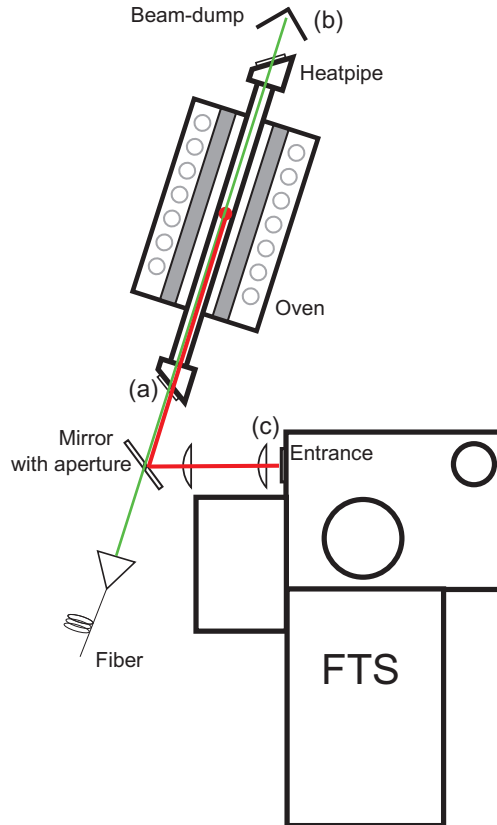


Figure 3.2.: Schematics of the heatpipe and Fourier-transform spectrometer. The laser is entering the heatpipe at point (a) and absorbed in a dark box behind it (b). The induced fluorescence is guided to the entrance of the Fourier-transform spectrometer (c) by means of a pierced mirror and two lenses.

approx. 1 litre per minute. The construction of tube and brass heads is sealed with uncoated glass windows, that give optical access for the laser. The tube can be evacuated and filled with rare gas atmosphere by means of a valve for control of noble gas pressure. Fig. 3.2 shows the experimental setup in a schematic with heatpipe oven, beam path and Fourier-transform spectrometer (FTS). Detailed drawings of the heatpipe-assembly can be found in [Hob06] and [All04].

The alkali metals were introduced into the heatpipe with a mixture of 30 % Na and 70 % K by weight. After evacuation we put Ar at a pressure of 5 mbar as a buffer gas inside the cell, which was heated up to 640 K. Two series of measurements were made:

1. We applied excitation of levels given in [Fer00] and [Kat90] with a Rhodamine 6G ring dye laser. In Fig 3.1 the solid line arrow shows the excitation into the $[B^1\Pi, c^3\Sigma^+]$ - manifold, the dotted line arrows represent the fluorescence into the singlet and triplet ground states. In Table 3.1 all used transitions are listed.
2. We repeated measurements by A. Ross described in [Ros85] with an Ar^+ laser in order to cover also the low v states $v_a = 1, 2, 3$ and higher rotational quantum numbers of the $a^3\Sigma^+$ state, $N_a = \mathcal{O}(60-70)$ ², and to check for consistent calibration in both experiments, because we wanted to include the data set from [Ros85] with the proper weights into our procedure. The excitation scheme is similar to the one in Fig. 3.1, but the upper states involved are the $D^1\Pi$ and $d^3\Pi$ states. The Ar-ion-laser was operated single-mode in the region of the 476 nm and 488 nm lines. A table with

²The symbol N is used for the Hund's case b triplet state because the total angular momentum J is the sum of N and spin S . [Her50]

v'	J'		v''	J''	ν (cm ⁻¹)
16	36	←	6	36	17019.136
4	13	←	0	14	17220.788
6	31	←	0	31	17314.689
8	46	←	0	45	17388.308
7	21	←	0	20	17389.252
8	8	←	0	8	17450.136
8	7	←	0	7	17450.802
8	6	←	0	6	17451.969
10	36	←	0	36	17502.082
10	35	←	0	35	17505.176
12	16	←	1	16	17507.824
10	35	←	0	34	17511.973

Table 3.1.: Experimentally verified transitions of the B¹Π←X¹Σ⁺ system excited with a single mode R6G ring dye laser.

wavenumbers can be found in [Ros85].

3.3. Experimental setup for LIF detection

The fluorescence was recorded with a Bruker IFS 120 HR Fourier-transform spectrometer with a resolution of 0.03 – 0.05 cm⁻¹. A schematic of the setup can be seen in Fig. 3.2: the heatpipe in its oven is placed on an optical table. The laser light is introduced out of an optical fibre into the cell (a) and absorbed on the rear part of the setup (b). The fluorescence light leaving the heatpipe at point (a) is collected into the Fourier-transform device via a specially prepared mirror and two lenses [All04].

A typical spectrum is shown in Fig. 3.3. One can see clearly

a long progression of the $X^1\Sigma^+$ state at the right side and a very narrow progression to the $a^3\Sigma^+$ state due to its shallow potential at the very left side. Already from one such spectrum the relative positions of the two electronic states are fixed due to the common upper level. The spectral region around 15798 cm^{-1} is not available in our measurements, because a notch filter suppressing the HeNe laser of the FTS cuts out also this part of the fluorescence light. Fig. 3.4 shows the range of (v, J) pairs obtained from all known observations used in the analysis, for both $X^1\Sigma^+$ and $a^3\Sigma^+$ states. For the triplet ground state we were able to find new important (v, J) combinations concerning the description of the joint progressions.

In the first series of measurements the argon buffer gas in the heatpipe allowed us to find rotational satellites of the strongest $X^1\Sigma^+$ lines in the spectra. Excitation of these lines should enable us to extend the range of data points in the J quantum number, which works fine to explore the singlet ground state. Unfortunately we had no success in finding more triplet levels with this method than shown in Fig 3.4. Satellite structures sometimes appearing within the triplet manifold could not be assigned. Hyperfine structure was not resolved, because the splitting is within the convolution of Doppler profile and apparatus function of the Fourier spectrometer.

3.4. Analysis

We started with the potential description given in [RA00] for the $X^1\Sigma^+$ state and in [Ros85] for the $a^3\Sigma^+$ state, and fitted analytical functions to the pointwise representations. The procedure is described in detail in earlier publications [Doc06, Pas07] and will be recalled here only in a short form: The complete potential en-

ergy curve is divided into a repulsive part $U_{SR}(R)$, an inner well $U(R)$ with a potential minimum and a long range part U_{LR} given by the following expressions:

$$U_{SR}(R) = A + \frac{B}{R^q} \quad \text{for } R < R_i \quad (3.1)$$

$$U(R) = \sum_{k=0}^n a_k x^k \quad \text{for } R_i \leq R \leq R_o \quad (3.2)$$

$$\text{with } x = \frac{R - R_m}{R + bR_m} \quad (3.3)$$

$$U_{LR}(R) = -\frac{C_6}{R^6} - \frac{C_8}{R^8} - \frac{C_{10}}{R^{10}} \pm E_{ex} \quad \text{for } R > R_o \quad (3.4)$$

where A , B and q are parameters, R_m is chosen close to the equilibrium internuclear distance, b is a parameter to control the pole position of the mapping function x of the infinite internuclear distance scale and allows for a steep slope for small internuclear separations ($R < R_m$) compared to large separations ($R > R_m$), a_k are the coefficients of the polynomial in x . R_i and R_o denote the connection points of the different branches. $C_{6/8/10}$ are the coefficients in the well known inverse power series for long range interaction and E_{ex} is the exchange term given by

$$E_{ex} = A_{ex} \cdot R^\gamma \cdot e^{-\beta R}, \quad (3.5)$$

with a negative sign for the singlet and a positive sign for the triplet state potential. The coefficients C_6 and C_8 are adopted from [Der01] and [Por03], respectively. C_{10} was used as a fitting parameter. γ and β for the exchange term were calculated from atomic ionization energies [Smi65] and kept fixed as well. Only the magnitude A_{ex} of the exchange term was varied. All three parts of the potential are connected continuously by selecting A and a_0 to enable us to solve the Schrödinger equation for the

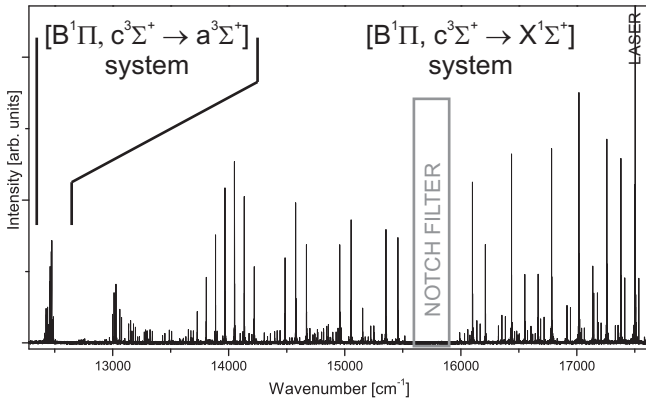


Figure 3.3.: The $[B^1\Pi, c^3\Sigma^+] \rightarrow X^1\Sigma^+$ and $[B^1\Pi, c^3\Sigma^+] \rightarrow a^3\Sigma^+$ bands of NaK excited with a single mode Rhodamine 6G ring dye laser at 17502.08 cm^{-1} . A notch filter in the spectral region around 15798 cm^{-1} suppresses the radiation of the reference laser of our Fourier-transform spectrometer and regrettably cuts out a part of the spectrum.

nuclear motion numerically. Damping functions [Tan84] were not introduced for changing over from the long range to chemically bound region because R_o was chosen sufficiently far out that all four terms in Eq. (3.4) together will represent the proper long range function with enough flexibility in fitting the data.

In a first approach the fits were done separately for the singlet and triplet manifold to save computing time and check the internal consistency of the data set. We added iteratively observed frequencies to the database, refining the description in this way. The initial singlet potential described our new results quite well.

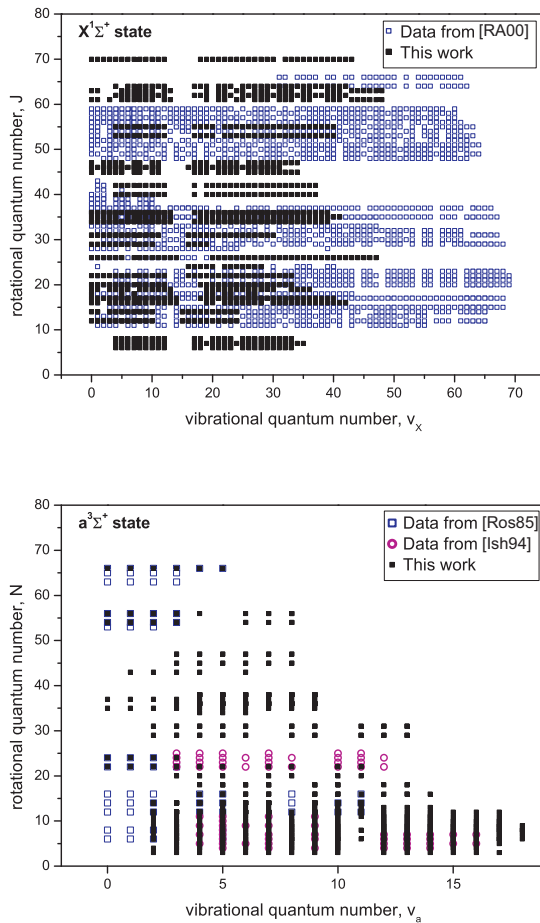


Figure 3.4.: The range of vibrational and rotational quantum numbers of the observed energy levels for both ground states. In the singlet state we mainly used the data set given by [RA00] complemented by our own data. For the triplet state our contribution is much more important, especially because primary spectral data from Ishikawa [Ish94] were not available for the present fitting procedure.

Table 3.2.: Parameters of the analytic representation of the potential energy curve for the $X^1\Sigma^+$ state of NaK. The potential is given with respect to the common asymptote $3s + 4s$. The coefficients of the of the power series (Eqs. 3.2 and 3.3) are listed in Table 3.2.

For $R < R_i = 2.53\text{\AA}$	
A	$-0.44525554 \times 10^4 \text{ cm}^{-1}$
B	$+ 0.107112840 \times 10^6 \text{ cm}^{-1} \text{\AA}^q$
q	8.3980
For $R > R_o = 11.3\text{\AA}$	
C_6	$0.1179302 \times 10^8 \text{ cm}^{-1} \text{\AA}^6$
C_8	$0.3023023 \times 10^9 \text{ cm}^{-1} \text{\AA}^8$
C_{10}	$0.9843378 \times 10^{10} \text{ cm}^{-1} \text{\AA}^{10}$
A_{ex}	$0.1627150 \times 10^4 \text{ cm}^{-1} \text{\AA}^{-\gamma}$
γ	5.25669
β	2.11445\AA^{-1}

The triplet potential required more changes, starting with the data from [Ros85] and adding new levels in order to find a proper description. From reference [Ish94] no experimental data were available to be included into our analysis. In the last step, the potentials were fitted simultaneously. Hereby the relative position of the two potentials became fixed, because many fluorescence progressions to the singlet and triplet states had common upper levels, and both potentials are joint with the same long range behaviour, as given by Eq. (3.4).

Hyperfine structure was not resolved with the used mode of operation of the Fourier-transform spectrometer. Some of the

triplet lines seem to show an asymmetric line profile. Thus we considered a correction to take care of the unresolved hyperfine structure in the fit (compare the procedure for KRb [Pas07]). But a simulation of line profiles overlapping the computed hyperfine structure showed that the correction is negligible. So we did not take this into account.

Tables 3.2, 3.3 and 3.4 show the final parameter sets, which allow for derivation of eigenenergies within the experimental uncertainty of 0.005 cm^{-1} (standard deviation of the fit $\sigma = 0.957$). The values of the a_k depend on the choice of b , R_m and the number of elements in the power expansion. A different choice would change the numerical values of a_k completely. To give an example: if one chooses R_m to be equal to the equilibrium internuclear distance R_e , a_1 would become exactly zero.

We did not calculate error limits for the coefficients a_k due to strong correlations between them and the dependence of their magnitude from the choice of the number of parameters. The number of digits given for each coefficient allows to describe our measurement data within the experimental uncertainty. Rovibrational energies can be calculated by the potential curves derived from the parameters in Tables 3.2, 3.3 and 3.4 with an accuracy not worse than 0.005 cm^{-1} for quantum numbers within the field represented in Fig. 3.4.

Data files with the observed transition frequencies and assignments are in the supplementary online material of [Ger08] for direct use in future analysis.

3.5. Results

Figure 3.5 shows differences $\Delta U(R)$ between earlier and present results for the potential energy curves of both ground states.

Table 3.3.: Parameters for the $X^1\Sigma^+$ state of NaK. (Continuation of Table 3.2.)

For $2.53\text{\AA} = R_i \leq R \leq R_o = 11.3\text{\AA}$	
b	-0.4
R_m	3.49901422 \AA
a_0	-5273.6205 cm^{-1}
a_1	-0.1254 cm^{-1}
a_2	$0.14536158 \times 10^5 \text{ cm}^{-1}$
a_3	$0.11484948 \times 10^5 \text{ cm}^{-1}$
a_4	$-0.3902171 \times 10^3 \text{ cm}^{-1}$
a_5	$-0.16931635 \times 10^5 \text{ cm}^{-1}$
a_6	$-0.374520762 \times 10^5 \text{ cm}^{-1}$
a_7	$0.106906160 \times 10^6 \text{ cm}^{-1}$
a_8	$0.5495867136 \times 10^6 \text{ cm}^{-1}$
a_9	$-0.2164021160 \times 10^7 \text{ cm}^{-1}$
a_{10}	$-0.10160808788 \times 10^8 \text{ cm}^{-1}$
a_{11}	$0.22144308806 \times 10^8 \text{ cm}^{-1}$
a_{12}	$0.10995928468 \times 10^9 \text{ cm}^{-1}$
a_{13}	$-0.15497420539 \times 10^9 \text{ cm}^{-1}$
a_{14}	$-0.782460886034 \times 10^9 \text{ cm}^{-1}$
a_{15}	$0.764737283856 \times 10^9 \text{ cm}^{-1}$
a_{16}	$0.3818679376129 \times 10^{10} \text{ cm}^{-1}$
a_{17}	$-0.270560881733 \times 10^{10} \text{ cm}^{-1}$
a_{18}	$-0.1307771478369 \times 10^{11} \text{ cm}^{-1}$
a_{19}	$0.6931241396136 \times 10^{10} \text{ cm}^{-1}$
a_{20}	$0.3179698977691 \times 10^{11} \text{ cm}^{-1}$
a_{21}	$-0.1275832531699 \times 10^{11} \text{ cm}^{-1}$
a_{22}	$-0.5474439830834 \times 10^{11} \text{ cm}^{-1}$
a_{23}	$0.1640384471424 \times 10^{11} \text{ cm}^{-1}$
a_{24}	$0.6534858404306 \times 10^{11} \text{ cm}^{-1}$
a_{25}	$-0.139350481085 \times 10^{11} \text{ cm}^{-1}$
a_{26}	$-0.5148927815627 \times 10^{11} \text{ cm}^{-1}$
a_{27}	$0.700666554236 \times 10^{10} \text{ cm}^{-1}$
a_{28}	$0.240949154116 \times 10^{11} \text{ cm}^{-1}$
a_{29}	$-0.15757958492 \times 10^{10} \text{ cm}^{-1}$
a_{30}	$-0.50725039078 \times 10^{10} \text{ cm}^{-1}$

Table 3.4.: Parameters of the analytic representation of the potential energy curve for the $a^3\Sigma^+$ state of NaK. The potential is given with respect to the common asymptote $3s + 4s$.

For $R < R_i = 4.55\text{\AA}$	
A	$-0.6838392 \times 10^3 \text{ cm}^{-1}$
B	$+ 0.281763541 \times 10^6 \text{ cm}^{-1} \text{\AA}^q$
q	4
For $4.55\text{\AA} = R_i \leq R \leq R_o = 11.3\text{\AA}$	
b	-0.66
R_m	5.47298825
a_0	$-207.7495 \text{ cm}^{-1}$
a_1	$0.104345 \times 10^2 \text{ cm}^{-1}$
a_2	$0.3811560 \times 10^3 \text{ cm}^{-1}$
a_3	$0.2432236 \times 10^3 \text{ cm}^{-1}$
a_4	$0.182422 \times 10^2 \text{ cm}^{-1}$
a_5	$-0.1183588 \times 10^3 \text{ cm}^{-1}$
a_6	$-0.5243827 \times 10^3 \text{ cm}^{-1}$
a_7	$-0.7362683 \times 10^3 \text{ cm}^{-1}$
a_8	$0.12436734 \times 10^4 \text{ cm}^{-1}$
a_9	$0.13720076 \times 10^4 \text{ cm}^{-1}$
a_{10}	$-0.40511451 \times 10^4 \text{ cm}^{-1}$
a_{11}	$-0.25977888 \times 10^4 \text{ cm}^{-1}$
a_{12}	$0.59928116 \times 10^4 \text{ cm}^{-1}$
a_{13}	$0.37710157 \times 10^4 \text{ cm}^{-1}$
a_{14}	$-0.29764114 \times 10^4 \text{ cm}^{-1}$
a_{15}	$-0.20459436 \times 10^4 \text{ cm}^{-1}$
For $R > R_o = 11.3\text{\AA}$	
C_6	$0.1179302 \times 10^8 \text{ cm}^{-1} \text{\AA}^6$
C_8	$0.3023023 \times 10^9 \text{ cm}^{-1} \text{\AA}^8$
C_{10}	$0.9843378 \times 10^{10} \text{ cm}^{-1} \text{\AA}^{10}$
A_{ex}	$0.1627150 \times 10^4 \text{ cm}^{-1} \text{\AA}^{-\gamma}$
γ	5.25669
β	2.11445\AA^{-1}

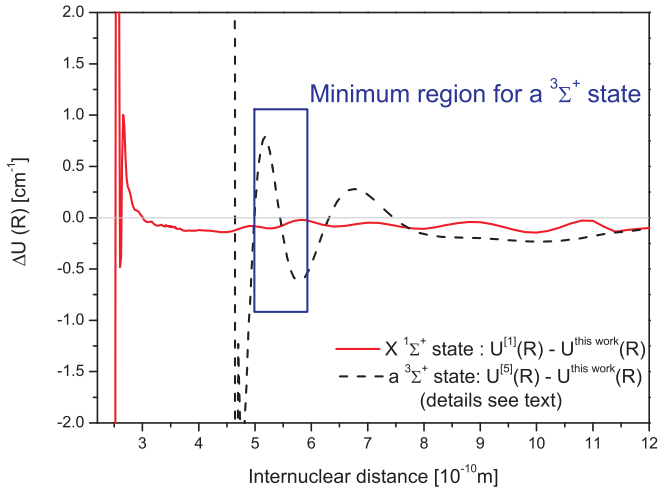


Figure 3.5.: Solid line: difference in energy between the result taken from [RA00] and our potential energy curve for the singlet state. Dashed line: same comparison for the triplet potential with [Ish94]. Here the differences are bigger due to bigger changes to the PEC during the refinement process described in section 3.4.

A comparison does not make sense in the inner repulsive part $U_{SR}(R)$ of the PECs, because the datafield does not contribute much to this form and because the slightest modifications of the steepness of these inner parts will only change the big amplitude of the oscillatory behaviour in the differences as can be seen in Fig. 3.5 to the very left, but will give no significant change in the energy level positions calculated with these potentials. Thus we consider for a comparison only the regions for $R > R_i$, where R_i is the connection point between $U_{SR}(R)$ and $U(R)$ (see Eq. (3.1))

and (3.2)) given in the headers of Tables 3.2, 3.3 and 3.4.

For the $X^1\Sigma^+$ state $R_i = 2.53 \text{ \AA}$ and the position of the potential minimum is $R_e = 3.4990 \text{ \AA}$, which is equal to the value found in [RA00]. The difference $\Delta U(R)$ is negative everywhere and does not exceed 0.15cm^{-1} for $R > R_e$.

For the $a^3\Sigma^+$ state the difference found above 5 \AA shows a magnitude of nearly one wavenumber (see highlighted box in Fig. 3.5). The potential minimum has a value of $R_e = 5.4475 \text{ \AA}$ in our work, which is 0.02 \AA smaller compared to the value from [Ish94]. The oscillatory behaviour of the difference in Fig. 3.5 around R_e results from these different potential minimum positions. A calculation of the difference in rotational constants for those different equilibrium internuclear distance positions shows for low J like 25 changes in the rotational energies of already 0.12 cm^{-1} , which is bigger than the experimental uncertainty obtained in our experiment. The levels with the higher J quantum numbers up to $J = 66$ for low v in this study fix the potential minimum much better than from the observations in [Ish94] where $J \leq 25$ were incorporated.

Table 3.5 compares selected equilibrium and long-range parameters of our PECs for both states with the values from earlier work.

The comparison of R_e and D_e values in Table 3.5 is mainly given by convention. The first problem with the derived constant D_e is the influence of uncertainties in the $C_{6/8/10}$ coefficients. This can be reduced when data from photoassociation experiments are available from ultracold ensembles. By this the dissociation limit is connected to a bound state level of the ground state via the two-photon photoassociation step. The second problem in comparing R_e and D_e is the model dependency of the PECs from the different mathematical representations of the functional form of the minimum. A way to avoid this problem is not to give D_e

Table 3.5.: Comparison of parameters used for our potential description compared to other works.

Parameter	This work	[RA00]	[Ish94]
$D_e^{(X)}$ (cm ⁻¹)	5273.62(10)	5273.696(45)	
$D_0^{(X)}$ (cm ⁻¹)	5211.75(10)		
$R_e^{(X)}$ (Å)	3.4990	3.4990	
$D_e^{(a)}$ (cm ⁻¹)	207.82(10)		207.858(19)
$D_0^{(a)}$ (cm ⁻¹)	196.48(10)		
$R_e^{(a)}$ (Å)	5.4475		5.4618
$10^{-7}C_6$ (cm ⁻¹ Å ⁶)	1.1793(120) •	1.2144(46)	1.275(15)
$10^{-8}C_8$ (cm ⁻¹ Å ⁸)	3.023(39) •	2.9619 •	2.22(19)
$10^{-9}C_{10}$ (cm ⁻¹ Å ¹⁰)	9.843	9.400 •	11.00(61)
A_{ex} (cm ⁻¹ Å ^{-γ})	1627.150	406642.6°	8.7×10^6 •
γ	5.25669	0	0
β (Å ⁻¹)	2.11445	0.9378903 [†] °	1.664 •
E_{ex} (cm ⁻¹)			
at $R_o = 11.3$ Å	0.023	0.043	0.059

• Values were fixed in the fit. For details, see discussion on C_n coefficients on page 50.

[†] Additional higher order terms in the exponential function of Eq. (3.5).

° The values for A and β are different to those found in [RA00] due to some unit conversion error in the original work as confirmed by the authors [Ros08].

but D_0 instead, the dissociation energy with respect to $v = 0$. This is a directly observable quantity, and therefore a much better choice than a model dependent constant. In Table 3.5 we give D_0 as well and want to encourage other authors to do the same in future publications for a more stringent comparison.

The errors of D_e and D_0 are determined by the uncertainty of the measured frequencies in our spectra, the error of the $C_{6/8/10}$ coefficients, the contribution of exchange energy and the model dependency as discussed before. The error of D_e is mainly determined by C_6 , while the experimental uncertainty and model dependencies can be neglected. The errors we obtain are higher than the ones given in [RA00] and [Ish94], but we want to point out, that the small uncertainty given in these papers might be doubtful considering the uncertainties and correlations of the $C_{6/8/10}$ coefficients (see discussion below).

For the C_n coefficients we took the most recent values to be found from [Der01] for $n = 6$ and from [Por03] for $n = 8$. The errors for C_6 and C_8 given in these papers are below 1% and 1.3%, respectively. The description with $U_{LR}(R)$ (Eq. (3.4)) begins at the connection point $R_o = 11.3 \text{ \AA}$ in our choice. From here to the dissociation limit the energy difference is about 7 cm^{-1} . The number of observed rovibrational levels contributing in this part of the potential curve is 4 for the $X^1\Sigma^+$ state and 34 for a $3\Sigma^+$ state. Due to these small numbers we do not fit the long range coefficients but use the theoretical values for two reasons: Firstly, it is not expected, that one can determine the long range function with such a small set of experimental values and thus within a small interval of internuclear distance. The C_n coefficients will be correlated, it will not be possible, to determine their values independently from each other. Secondly, the selected coefficients C_6 and C_8 are significantly less dependent from theoretical estimates and their uncertainty is sufficiently low to allow spectral

i	Y_{i0}	Y_{i1}	Y_{i2}
0		0.0393984(28)	-0.51470(70)E-06
1	23.0099(14)	-0.125123(81)E-02	
2	-0.62169(25)	0.197(15)E-05	
3		-0.18082(71)E-05	-0.1835(19)E-08
4	-0.2627(54)E-03		0.1682(17)E-09
5	0.2528(66)E-04		
6	-0.1623(32)E-05		-0.3502(25)E-12
7	0.4811(56)E-07		

i	Y_{i3}	Y_{i4}
2	-0.2588(17)E-11	
3	0.8593(81)E-12	-0.3962(59)E-16
4	-0.6040(52)E-13	

Table 3.6.: Dunham-type coefficients [Tow75] for the $a^3\Sigma^+$ state of $^{23}\text{Na}^{39}\text{K}$, valid for $v \leq 18$ and $J \leq 66$. All values in cm^{-1} . This set reproduces the term energies within 0.005 cm^{-1} .

predictions with the accuracy of the present experiment.

Only the C_{10} parameter was fitted, mainly to get a smooth connection between the inner well and the long range part of the potential curve. But the obtained C_{10} parameter, $2.60 \cdot 10^7$ in atomic units, agrees well with the theoretical value in [Por03] within its stated error limit of 10%.

In contrast, Ishikawa fitted all C_n parameters to the IPA curve obtained by molecular spectroscopy in an interval of $R = 7.6 \text{ \AA}$ to $R = 14 \text{ \AA}$ and got errors in the same order of magnitude compared to the theoretical values. But the reported values (see right column in Table 3.5) are outside the uncertainty limits of the

theoretical estimates and thus the close coincidence of the dissociation energy of their study and ours for the triplet state is probably by chance indicating the already mentioned correlation of the C_n coefficients.

In the work of Russier-Antoine [RA00] C_8 and C_{10} are kept at theoretical values from [Mar99], where no error limits are given. Only C_6 is fitted to the long range part of the derived IPA curve obtained there and to 188 measured term energies in the interval of $R = 8 - 11.5 \text{ \AA}$, thus giving them a special weight in the evaluation. Considering that the LeRoy-radius is 10.8 \AA [Ish94] for NaK, we doubt that such fits [Ish94] and [RA00] lead to better values for the long range coefficients, because the exchange contribution might not be well represented by the functional form at the lower limit of the applied ranges. Those exchange energy parameters are also given in Table 3.5. In our model the long range description starts at $R = 11.3 \text{ \AA}$ beyond the LeRoy-radius, where the contribution of the exchange term is only 0.023 cm^{-1} (see also Table 3.5 for comparison at this specific internuclear distance).

In Table 3.6 we give an updated set of Dunham coefficients for convenient, future spectroscopy of the triplet ground state. It improves the most recently published set in [Ros85]. To fit the Dunham ansatz to the experimental data, it was necessary to consider only line differences within the $a^3\Sigma^+$ state, because the excited $B^1\Pi$ is strongly perturbed, which made a Dunham fit of the combined system impossible. The new set of Dunham coefficients reproduces the term energies of the triplet state within the averaged experimental uncertainty of 0.005 cm^{-1} . The standard deviation of the fit is $4.9 \times 10^{-3} \text{ cm}^{-1}$ and the normalized value is $\sigma = 0.85$.

Table 3.7.: Scattering lengths for the $X^1\Sigma^+$ and $a^3\Sigma^+$ molecular states of the various isotopic combinations of NaK compared to results from [Ven01]. All values are given in Bohr radii ($a_{\text{Bohr}} = 0.5292 \times 10^{-10}\text{m}$). The maximum v quantum numbers given are supported by rotationless potentials from this study for the different isotopologues.

	Venturi et al. [Ven01]		This work	
	singlet	triplet	singlet	v_X^{max}
$^{23}\text{Na} - ^{39}\text{K}$	$3203 \pm \infty$	-27^{+7}_{-8}	393^{+105}_{-68}	74
$^{23}\text{Na} - ^{40}\text{K}$	76^{+11}_{-9}	-129^{+28}_{-40}	69^{+1}_{-2}	74
$^{23}\text{Na} - ^{41}\text{K}$	17^{+11}_{-14}	$3625 \pm \infty$	$6.4^{+3.0}_{-3.5}$	74
				v_a^{max}
$^{23}\text{Na} - ^{39}\text{K}$				19
$^{23}\text{Na} - ^{40}\text{K}$				19
$^{23}\text{Na} - ^{41}\text{K}$				20

The limits given for the values of this study are not uncertainties, but determined by a variation of C_6 within the limits given by theoretical predictions and refitting the potentials. For details see text.

3.6. Cold Collisions

Table 3.7 presents the values for the singlet and triplet scattering lengths of NaK calculated in [Ven01] in comparison with the values found in this study. It also shows the maximum vibrational quantum number supported by the potentials for the different isotopes in the rotationless case. The v_{max} are identical to the prediction in [Ven01].

The agreement for the singlet scattering length is good considering the error limits given by [Ven01] and reflects, that there are

no major changes to the potential energy curve of the $X^1\Sigma^+$ state compared to the work of [RA00], which was used by the authors of [Ven01]. Surprisingly, the use of different $C_{6/8/10}$ coefficients [Mar99] instead of [Der01, Por03] is not influencing the values of the scattering length, which might be again a result from the correlation between the C_n coefficients, e.g. C_6 shows an opposite magnitude ratio between the values from theory and those from [Ven01] than C_8 does (see Table 3.5).

For the triplet scattering lengths the values do not agree. We already saw, that the triplet curves are mainly shifted in the region of the potential minimum and show better agreement in the asymptotic region despite different $C_{6/8/10}$ coefficients. To illustrate the strong dependency on the $C_{6/8/10}$ coefficients and to give intervals for the scattering lengths derived here, we varied the magnitude of C_6 within the error limits given in [Der01] and fitted the potentials again by only varying C_8 . The fit quality was as good as before, which proves the strong correlation between the C_n coefficients. With the modified potentials we calculated the scattering lengths again. The obtained intervals of the scattering lengths can be found in Table 3.7. We want to emphasize that these are no real error limits, but only give an impression, how sensitive the scattering lengths react on allowed changes of the potential form within the theoretical estimates.

A scattering calculation with magnetic fields was started to predict interesting B-field regions for experiments working with ultracold ensembles: For the lowest atomic asymptote all three isotopologues have at least one s-wave resonance for magnetic fields below 500 G and with a tuning width of several G. For $^{23}\text{Na}^{40}\text{K}$ and $^{23}\text{Na}^{41}\text{K}$ resonances below 100 G were found. This fact is very promising for experiments with ultracold Na and K collisions.

3.7. Potentials for beam experiments

The motivation for the heatpipe study was already given at the beginning of this chapter. In addition to these arguments the potential curves obtained are extremely useful for the beam experiments, which will be presented in Chapter 4.

The high resolution spectroscopy, that is possible with such a machine, requires an extreme precise potential information. For an excitation spectroscopy the structure of both molecular electronic states involved (ground state and excited state) must be known in order to understand the observed spectra.

The excitation laser is tuned and scans over the rovibrational levels of both states. Due to the limited scanning range of a laser of typically 15 GHz only a small part of the rovibrational structure can be seen in each scan. In order to analyse the spectra a good prediction is indispensable. A study of the excited state is only possible, if sufficient information about the ground state(s) is existent.

In this respect the heatpipe study is of great value for the following experimental steps and was intended to precede the build-up of the beam apparatus.

MOLECULAR BEAM SETUP

A new beam apparatus was built up from scratch. In contrast to the heatpipe setup, where the Doppler effect causes a line width of typically 1 GHz for NaK heated to 600 K, the Doppler width is reduced to several MHz by collimation of the beam. A similar high resolution could be achieved by using polarization spectroscopy [Kas91], but the beam has the advantage of more than one possible interaction zone spatially separated. Franck-Condon-Pumping or STIRAP (Stimulated Raman Adiabatic Passage) can be applied in a first zone and detection or state analysis at a different place.

The high resolution is necessary for experiments like Stark spectroscopy (Chapter 5). According to Fig. 2.5 and Eqs. (5.1) to (5.3) a typical electric field of 2 kV will produce a level splitting of 300 MHz for the $B^1\Pi$ state (linear Stark effect) and only 50 MHz for the $X^1\Sigma^+$ state (only quadratic Stark effect). Thus in a simple heatpipe setup these effects could not be observed.

An oven design was implemented, where the heaters are placed outside the vacuum. It was developed to investigate earth alkaline

dimers at temperatures above 1300 K. These experiments were not successful, only the Ca atomic signal on the intercombination line of several isotopes was seen [Fal07].

With this beam chamber the oven concept was tested extensively with the heteronuclear dimer NaK. First tests, characterization of the beam and systematic excitation spectroscopy of NaK will be described in this chapter.

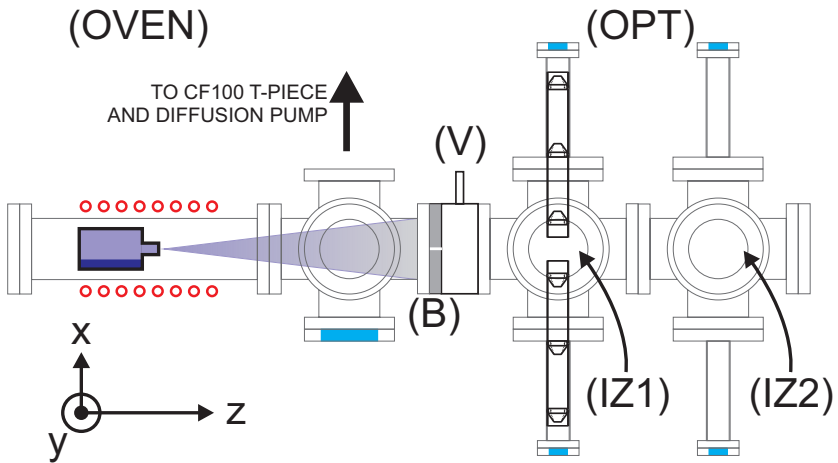


Figure 4.1.: Top view (simplified) on the vacuum chamber: The atomic/molecular beam propagates in z -direction. The modified blind (B), valve (V) and aperture rods (in the optics part OPT, see Sec. 4.3) are pronounced, oven container and heating elements only implied. The interaction zone (IZ2) was not used until implementation of electric field plates (Chapter 5).

4.1. Chamber design

A sketch of the new apparatus can be seen in Fig. 4.1. For reasons of costs and time it was completely built from standard vacuum components namely: three six-way CF100 crosses, four CF100-CF40 reducer flanges, one CF100 T piece, the tube that contains the oven (CF100 full nipple), a CF100 UHV-valve (V) that separates the oven part (OVEN) of the chamber from the optics part (OPT), two 3xCF40 on CF100 cluster-flanges, several windows and blinds.

The oven part is pumped by a diffusion pump (Model: Edwards Diffstak 160-700), which is pumped by a Varian DS602 rotary pump. The optics part is pumped by a turbomolecular pump (Varian T-V301 Navigator) backed by a Varian DS102 pump. Pressure detection in both part is accomplished by two Leybold cold cathodes controlled by the Leybold Center Three Unit, which are mounted at the cluster flanges. Ultimate vacuum conditions for oven and optics parts are $5 \cdot 10^{-7}$ mbar and $6 \cdot 10^{-8}$ mbar respectively. With running experiment (oven heated, alkali vapor) the pressure in the oven part goes up to $3 \cdot 10^{-6}$ mbar.

4.2. Molecular beam source

The end-tube in the oven part of the chamber contains a sample source with a nozzle of 200 μm . Its development is described in [Fal07]. The container can be removed for refill by opening the CF100 blind at the rear side of the vacuum tube (Fig. 4.2).

The oven container itself is sealed with two CF40 flanges. The blind flange at the back side is for refill. The front flange bears the nozzle in its center. The container fits exactly into the inner diameter of the vacuum tube. Thereby the nozzle position is

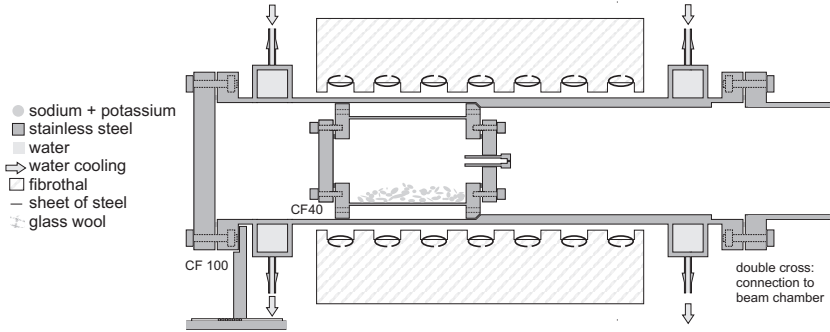


Figure 4.2.: Drawing of the oven construction, reprinted from [Fal07] Fig. 6.2(a). The sample container can be filled via the CF40 end flange. In the middle of the front flange sits the $200\mu\text{m}$ laser drilled nozzle for supersonic expansion. The whole container is placed inside the vacuum such that the nozzle is at mid of the oven shells which surround the vacuum tube where the temperature is highest.

always aligned to the center as long as the vacuum chamber is aligned.

Heating is accomplished with two resistance heaters (in form of two half-cylinder shells). By construction the middle of the heating elements is the hottest point, where the nozzle sits. Two cooling rings at the ends of the vacuum tube allow set up of a temperature gradient. Cooling can be done via air flow or with water directed through the cooling rings.

Temperature is measured via K-type thermocouples placed in small drilled holes at positions of nozzle and back flange, which is the coolest part of the oven oven and determines the vapour pressure.

When the oven is heated, a beam of atoms and molecules emerges into the vacuum. It is collimated by a modified blind (B) with a hole of 2 mm next to the valve (V) in the oven part. The beam

then enters the optics part and can interact with laser light at right angle (Fig. 4.1, x -direction). From the distance $b = 500$ mm of the modified blind (aperture) to the nozzle and the diameter $d = 2$ mm of the aperture one can derive the collimation ratio, which determines the reduction of the Doppler width

$$\tan(\epsilon)^{-1} = \frac{2b}{d} = 500. \quad (4.1)$$

4.3. Optical system and photomultiplier

Fig. 4.3 shows the optical system in the first interaction zone (IZ1). When the laser light hits an atomic or molecular resonance, the fluorescence light is collected by a spherical mirror M ($f = 19$ mm) and two lenses inside the vacuum (L1: $f_1 = 60$ mm, L2: $f_2 = 75$ mm). A third lens ($f_3 = 125$ mm) outside vacuum focusses the image onto the sensitive area of a photomultiplier (Hamamatsu R943-02). The optical traces were optimized with the LINOS WinLens software [Win06]. Exact measures and distances can be found in [Ste06].

The Signal-to-background ratio was greatly improved by implementing the two aperture rods (of length $l = 277.5$ mm) to reduce stray light after the first bandhead was recorded (Sec. 4.6). The design followed the idea given in [Jun06]. They were produced to fit exactly into the reducer flanges (outer diameter $d_{out} = 36.7$ mm). The inner diameter of the single aperture is 10 mm. They are made of aluminium which was anodized in black. With this improvement no filters at all were used to record the spectra for the systematic bandhead spectroscopy (Sec. 4.7).

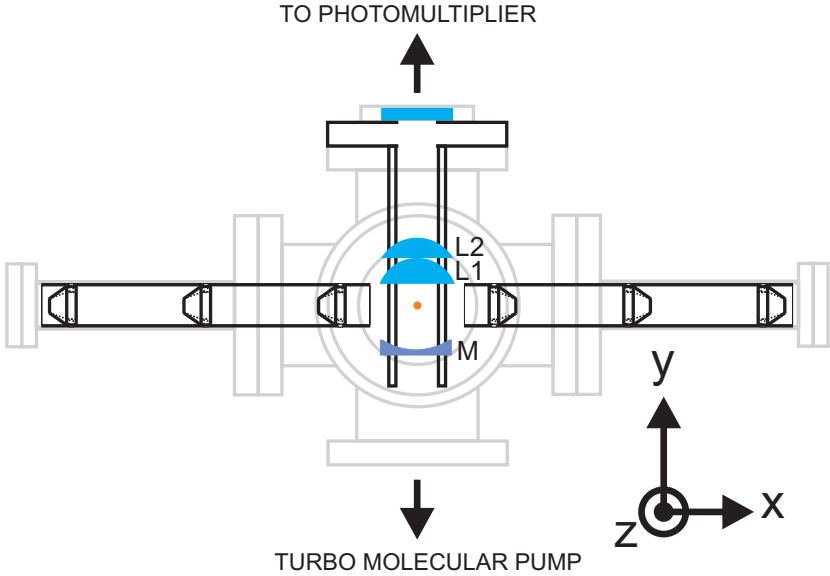


Figure 4.3.: Optical system in the first interaction zone (IZ1). Mirror and lenses are mounted using the Thorlabs two inch cage system. The third lens outside vacuum is not shown. It is mounted in a constructed adaptor, which is located between the vacuum chamber and the photomultiplier cooling housing.

4.4. Rotational temperature of the potassium dimer

The first tests of the system were taken with known lines. After filling the oven container with potassium only the D-lines [Fal06b] were found on the first run and used to optimize the geometry in particular the adjustment of the laser beam through the interaction zone (IZ1). The chamber itself is adjusted by the CF-connections of the vacuum elements, everything is centred au-

tomatically.

The next step was to take known molecular lines of the potassium dimer. Observed bandheads are listed in the appendix of [Lis01a]. The molecular signal is much weaker compared to atomic signals, because most molecules run only through a single cycle of excitation and fluorescence. For the same reason, (optical) cooling of molecules is so difficult, because there are no closed cooling cycles [Zep09]. The molecular K_2 signal was found after some optimization of oven temperature and gradient and employment of several filter combinations to reduce stray light.

Several R-lines of the K_2 A - X (18 - 0) band were measured and allowed to determine the rotational temperature of the beam. The intensities of the lines are described by a product of population of the initial state, the Hönl-London factor (HL) and the Franck-Condon factor (FCF):

$$I \sim n(E) \cdot (HL) \cdot (FCF) \quad (4.2)$$

The Franck-Condon factor for a given band is assumed to be constant for low J . The Hönl-London factor for R(J)-transitions is for a $^1\Sigma - ^1\Sigma$ band

$$(HL) = \frac{J + 1}{3(2J + 1)} \quad (4.3)$$

for pure BO-states with no perturbation. Assuming a Boltzmann distribution for the population

$$\begin{aligned} n(E) &= g \cdot C_0 \cdot \exp\left(-\frac{E}{kT}\right) \\ \text{with } E(J) &= B_{v''} J(J + 1) \end{aligned} \quad (4.4)$$

where g is the factor of degeneracy, $g = 2J + 1$, k the Boltzmann constant, $B_{v''}$ the rotational constant of the ground state,

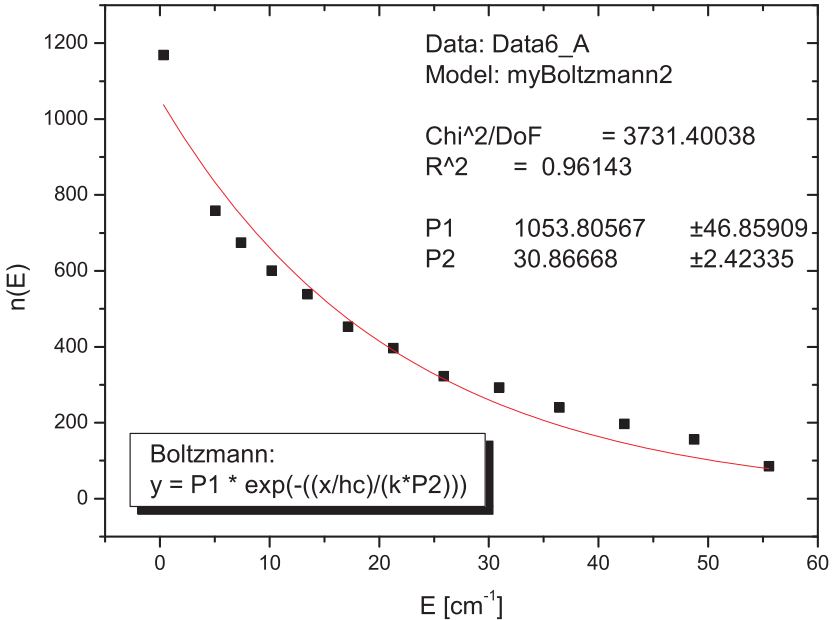


Figure 4.4.: Rotational temperature determined with rotational lines of the K_2 A - X (18 - 0) band. Line intensities were divided by the proper Hönl-London factors and degeneracy multiplicity leaving the Boltzmann distribution of population. Explanation of the variables in the inlay: the fitted constant P1 contains factors from Eqs. (4.2) and (4.4), P2 is the fitted temperature and variable x corresponds to the energy on the abscissa.

one can fit the observed intensities to the exponential function to obtain the rotational temperature. Fig. 4.4 shows the experimental data with the fitted curve. The temperature out of the fit is $T_{rot} = 31 \pm 3 K$, but line intensities for lines with sufficient S/N ratio can be measured with an uncertainty of $\sim 10\%$ only, there-

fore it is estimated that $T_{rot} = 30(10) K$. This shows, that indeed a cooling of internal degrees of freedom has taken place, which is a characteristic of supersonic expansions. Measurements of transitions starting from $v = 1$ and $v = 2$ in the ground state allowed to calculate the vibrational temperature of $T_{vib} = 40(10) K$ in a similar manner. Here only three data points were taken, what makes such a fit already questionable. Molecules initially in the $v = 3$ states were not found. Most molecules in the beam are in the vibrational ground state.

NaK molecules were found in the beam after several days of trying. Here no listed transitions for small J quantum numbers were available from the literature, and we had to rely on the description of the $X^1\Sigma^+$ ground state, which was presented in Chapter 3, and the excited state $B^1\Pi$, where a set of Dunham coefficients was used, that can be found in [Kat90]. To predict transition frequencies one needs sufficient knowledge about both states.

4.5. Velocity of the molecular beam

To characterize the molecular beam further, the particle velocity was measured by a Doppler shift experiment. The principle of measurement can be found in [Sco88] (\rightarrow Sec. 23.3.2).

Fig. 4.5 shows the experimental setup. After crossing the molecular beam at right angle (a) the excitation laser was redirected via two mirrors and crossed the molecular beam a second time with an angle $\beta > 90$ (b). For this purpose the reducer flanges in the first interaction zone were replaced by CF100 windows for that measurement day, which allowed for higher crossing angles. A molecular transition at frequency ν_0 for beam (a) will

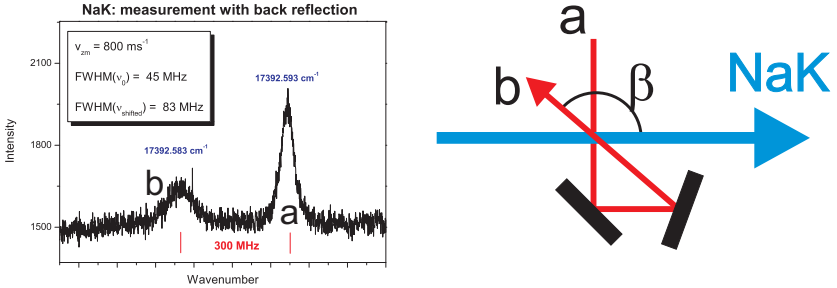


Figure 4.5.: Setup for the Doppler measurement with laser beams (a) and (b) crossing the molecular beam.

be Doppler shifted for beam (b)

$$\Delta\nu = \frac{v_{Mol}}{c} \cdot \nu_0 = \frac{v_z \cos(\beta)}{c} \cdot \nu_0 \quad (4.5)$$

With $\beta > 90$, the second component (b) in the scan will be shifted by $\Delta\nu$ to lower frequencies. The collimation of the molecular beam vertical to the direction of propagation of NaK molecules (z -axis in Fig. 4.5) leads to a reduced velocity distribution compared to the z -direction. Therefore the additional component is not only shifted but also broadened. Figure 4.5 shows the recorded scan over R(17) line in the NaK B – X 7 - 0 band with the shifted and broadened component. Calculation of v_z with $\beta = 102.53$ for the observed shift gives $v_z = (800 \pm 100)$ m/s.

4.6. NaK - the first bandhead

After measurements of a few rotational lines and determination of rotational temperature and beam velocity a full bandhead was scanned for $J = 0..15$. The excited state is a Π state, so P, Q and R lines are allowed from selection rules [Her50]. From the

heatpipe study the perturbed lines were already known, in that case they were used to find progressions into singlet and triplet ground states simultaneously (see Chapter 3). The search for an unperturbed bandhead began, to make the line assignment and orientation in the spectra easier.

The NaK B – X 11 - 0 band was the first bandhead that was assigned completely. Figure 4.6 (a) shows the range of 15 wavenumbers that had to be scanned for this. The R6G dye laser used for this purpose was not able to scan the whole interval at once, but allowed a maximum scanning range of 20 GHz (0.6 wavenumbers). So the spectrum in Fig. 4.6 (a) is composed of many single scans. The dotted lines show an overlay of a fluorescence progression with rotational satellites from higher J of the same band that was taken in the pre-study in the heatpipe. This coincidence helps in the assignment. The arrow points to the position of the bandhead. To higher wavenumbers there are still lines appearing, which belong to other bands. The difference in background from 17595 cm^{-1} on is due to a different measurement day with slightly different stray light conditions. Fig. 4.6 (b) is a zoom of the bandhead with assigned quantum numbers. The second band overlapping the structure is the NaK B – X 14 - 1 band.

4.7. Systematic exploration of the B state in NaK

Once a vibrational band was completely scanned and assigned, this was continued for the lowest vibrational bands of the $B^1\Pi$ state from $v = 1$ up to $v = 15$. Unfortunately the gain profile of the R6G dye did not support scanning of the NaK B-X 0-0 band. The 15-0 and 16-0 band were measured with R110, but the laser was unstable as well in the necessary spectral range. Scanning of the

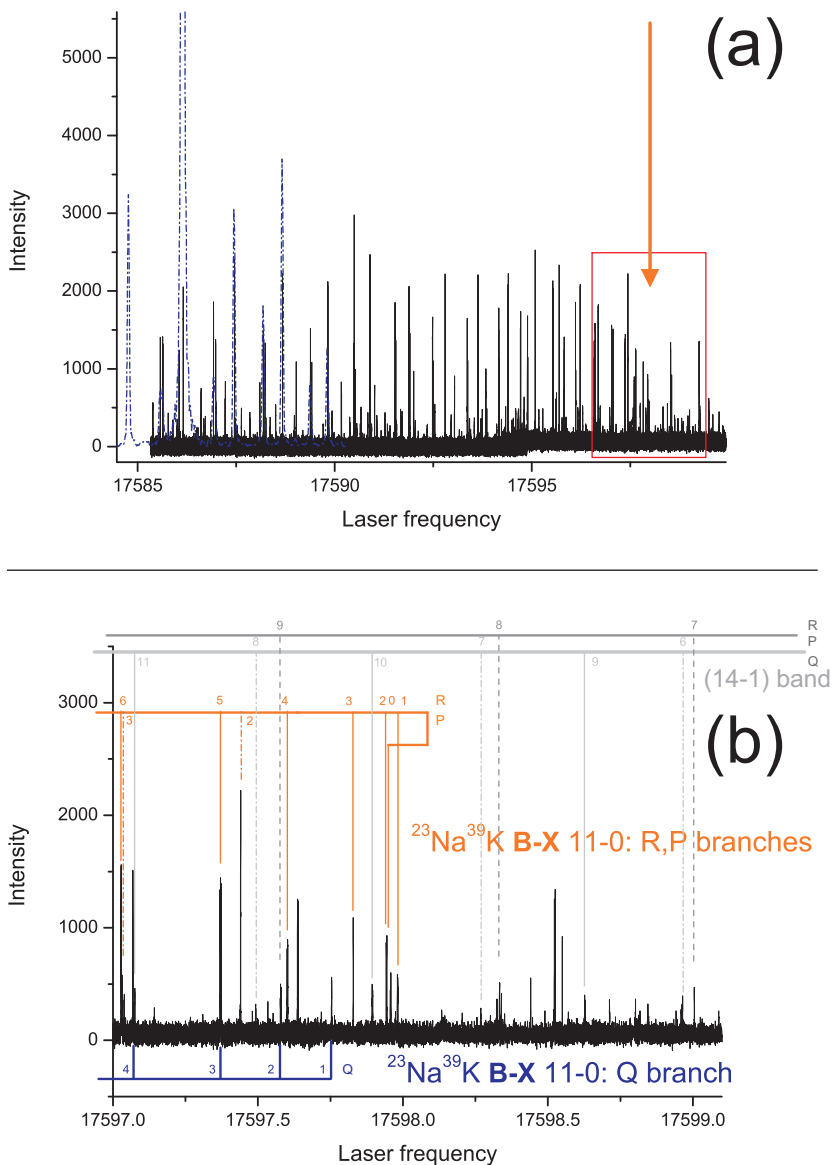


Figure 4.6.: The first complete bandhead: NaK B – X 11 – 0. (a) Complex spectrum from overlapping bands, the dotted curve shows rotational satellites from a heatpipe spectrum. (b) Zoom of the right side in (a) showing the bandhead.

16-0 band was cancelled.

The list of transitions is tabulated in Appendix A for each band. Assignment for the highly perturbed bands was sometimes not possible with the given Dunham description, so the bands 4-0 and 8-0 are missing in the collection (measurements and line positions are available but not assigned). The 12-0 band has been fully recorded, but the experimental circumstances for the reference trace for I₂ were so noisy, that an evaluation was not possible up to now.

The B¹Π state has been described by Katô *et al.* [Kat90], who applied a de-perturbation treatment to derive molecular constants for $v = 0..16$ and described the perturbation between the B¹Π state and c³Σ⁺ state for each band. Kasahara *et al.* [Kas91] even extended the description of the B¹Π state up to the dissociation limit. The B¹Π - X¹Σ⁺ transitions of ²³Na³⁹K were in both cases measured by optical-optical double resonance (OODR) polarization spectroscopy. The de-perturbation was done locally, i.e. band by band. Recently the primary input data of [Kat90] was kindly provided by the authors [Kas09]. After assignment of the perturbed bands from beam spectroscopy this very precise spectroscopic information can be used to start a global de-perturbation analysis with the Fourier grid method as done e.g. for K₂ [Lis01b].

The direct use of the measured transitions within this thesis was the search for well isolated lines to perform a Stark spectroscopy on them (Chapter 5). In general every line can be a candidate for an electric field measurement, no matter how many lines are in the neighbourhood, but since all lines will show a Stark splitting (the size and splitting manifold, i.e. number of subcomponents, depend on the J quantum number), the resulting spectra can get pretty dense and difficult to assign. Therefore the search for separated lines began. Four very suitable transitions in three different

bands were found and surveyed. In this respect the elaborate spectroscopy turns out to be very useful.

4.8. A comment to the oven concept

Although the oven proved to work fine and produced molecular signals with a signal to noise ratio of ≈ 50 for the stronger molecular lines, there are some design flaws that should at least be mentioned:

- The temperature measurement is done via K-type thermocouples (Sec. 4.2), but for geometrical reasons, they need to be introduced to the container from the nozzle side. This might lead to a thermocouple wire hanging in the molecular beam path after heating up, with the result that no signal can be seen or the signal is reduced due to this block. It happened several times, that a measurement day had to be cancelled, and at a later stage the thermocouples were removed completely, because the temperature turned out to be very reproducible by setting the voltage of the resistance heater. Indicator for a good beam condition and similar temperatures compared to before was then an atomic or molecular line that was known from earlier measurements.
- The oven has only one temperature to adjust. There is no separated heating of the nozzle, which turned out to be of disadvantage. In principle not possible by design, the nozzle clogged from time to time (even when it is always the hottest point of the setup), which could be turned around by applying a short voltage/temperature ramp to free it. But this did not always work. The gradient can be modified by the water flow through the cooling tubes, but this has limits

as well. From experience and from the experimental point of view several adjustable temperatures are favourable.

- The one container concept did only work out, because Na and K have very similar vapour pressure curves [Nes63]. For other heteronuclear combinations an oven with two reservoirs should be considered (see Outlook Chapter 6).

STARK EFFECT MEASUREMENTS

Electric field plates were introduced into the molecular beam chamber in order to measure electric dipole moments and to test the vibrational dependence of the electric dipole moment function for NaK predicted by the theoretical approach in Chapter 2. The formulas for the shifts of energy levels in the B $^1\Pi$ state and the X $^1\Sigma^+$ state will be introduced before the modification of the beam apparatus is described.

Three vibrational bands were measured to compare with the theoretical prediction. The evaluation of the spectra, a discussion of the uncertainties and comparison with theory will show a very good agreement when a scaling factor is applied.

5.1. Stark shift formulas

The expression for the linear Stark effect of a diatomic molecule is given in [vV65] (here the rewritten to get the energy shift in wavenumbers):

$$\begin{aligned}\Delta E^{(1)}(J, M) &= -\frac{1}{hc} \frac{M\Lambda}{J(J+1)} (\mu_v E) \\ &= -f(J, M) \cdot (\mu_v E),\end{aligned}\quad (5.1)$$

where J is the rotational quantum number of the state under consideration, M the projection of rotation on the quantization axis, E is the electric field strength, μ_v the permanent electric dipole moment of a given vibrational state v , and Λ the quantum number of the projection of the total electronic orbital angular momentum onto the molecular axis. Σ states do not show any linear Stark effect ($\Lambda = 0$). Thus we have to go to higher order perturbation theory to describe the Stark effect of the the ground state being $X^1\Sigma^+$. This order will also be needed for the state $B^1\Pi$, because we will apply high electric fields for splitting the rotational levels of the ground state. The second order contribution for a vibrational state with rotational constant B_v writes [vV65]:

$$\begin{aligned}\Delta E^{(2)}(J, |M|^2) &= \frac{1}{2hcB_v} \left[\frac{(J^2 - M^2) \cdot (J^2 - \Lambda^2)}{J^3(2J-1)(2J+1)} \right. \\ &\quad \left. - \frac{[(J+1)^2 - M^2] \cdot [(J+1)^2 - \Lambda^2]}{(J+1)^3(2J+1)(2J+3)} \right] (\mu_v E)^2 \\ &= g(J, |M|^2) \cdot (\mu_v E)^2\end{aligned}\quad (5.2)$$

and turns for $\Lambda = 0$ (and $J \neq 0$) into

$$\begin{aligned}\Delta E^{(2)}(J, |M|^2) &= \frac{1}{2hcB_v} \left[\frac{J(J+1) - 3M^2}{J(J+1)(2J-1)(2J+3)} \right] (\mu_v E)^2 \\ &= h(J, |M|^2) \cdot (\mu_v E)^2\end{aligned}\quad (5.3)$$

The functions $f(J, M)$, $g(J, |M|^2)$ and $h(J, |M|^2)$ display the quantum number dependence and contain in this definition some constants to get the shift in units of wavenumbers.

During planning stage of the experiment the above equations were used to estimate the field strength needed to observe splittings that can be detected with the resolution that is determined by the collimation ratio of the beam (Chapter 4.2). Input data were the dipole moment functions that were calculated for this purpose (Chapter 2.5) and the rotational constants for the vibrational levels [Kat90]. A typical electric field of 2 kV will produce a level splitting of 300 MHz for the $B^1\Pi$ state (linear Stark effect) and 50 MHz for the $X^1\Sigma^+$ state (only quadratic Stark effect). The chosen collimation ratio gives rise to a spectral resolution of a few MHz, which will be sufficient to detect the effect and to measure the Stark shifts for the excited and ground states with a relative accuracy up to 10^{-2} and 10^{-1} respectively.

During evaluation of the experimental spectra (Sec. 5.5) the above equations were used to calculate the energy shifts and fit them to the experimental observation. The accessible quantity to be fitted is the product $(\mu_v E)$. For higher values of the electric field the agreement between calculation and observation got worse. Polarization effect might be considered by an additional contribution, which is also second order in electric field (αE^2). For Σ states it writes [Dij71]:

$$\Delta E_{\Sigma}^{(pol)}(J, |M|^2) = -\frac{1}{2}(\alpha_{\parallel} - \alpha_{\perp}) \frac{2J(J+1) - 2M^2 - 1}{(2J-1)(2J+3)} E^2 \quad (5.4)$$

where α_{\parallel} and α_{\perp} are polarizabilities parallel and perpendicular to the molecular axis. Only the difference is accessible in this experiment. The M dependence is very similar to Eq. (5.3) and only the difference in the denominator can serve for distinguishing between dipole moment and polarizability. Thus one has to make a series of measurements at high fields with different J .

5.2. Design of electrodes

The electric field plates for the Stark measurement are suspended inside the vacuum chamber from a CF100 blind, that holds standard components from Thorlabs. They lead over to a Teflon construction of four solid rods which hold the Teflon sockets, where the stainless steel electrodes are mounted in (Fig. 5.1). The electrodes are produced with a surface roughness better than 0.01 mm on their whole area of $\pi \cdot (10 \text{ mm})^2$. Adjustment is done via a M20x1 thread of the electrodes in the sockets, which allows for a distance reproducibility of at least 50 μm . The relative uncertainty in distance is therefore $50 \mu\text{m}/10 \text{ mm} = 5 \cdot 10^{-3}$. The exact distance of 10mm between the two field plates is calibrated with an optical etalon made of CERODUR. Its width is $(10.000 \pm 0.001) \text{ mm}$, taken from an ULE cavity spacer.

In the design stage of the electrodes small surface roughness and distance uncertainty were intended to provide an electric field, with field variation smaller than 1% to avoid line broadening or line asymmetry, which would corrupt the achieved spectral resolution.

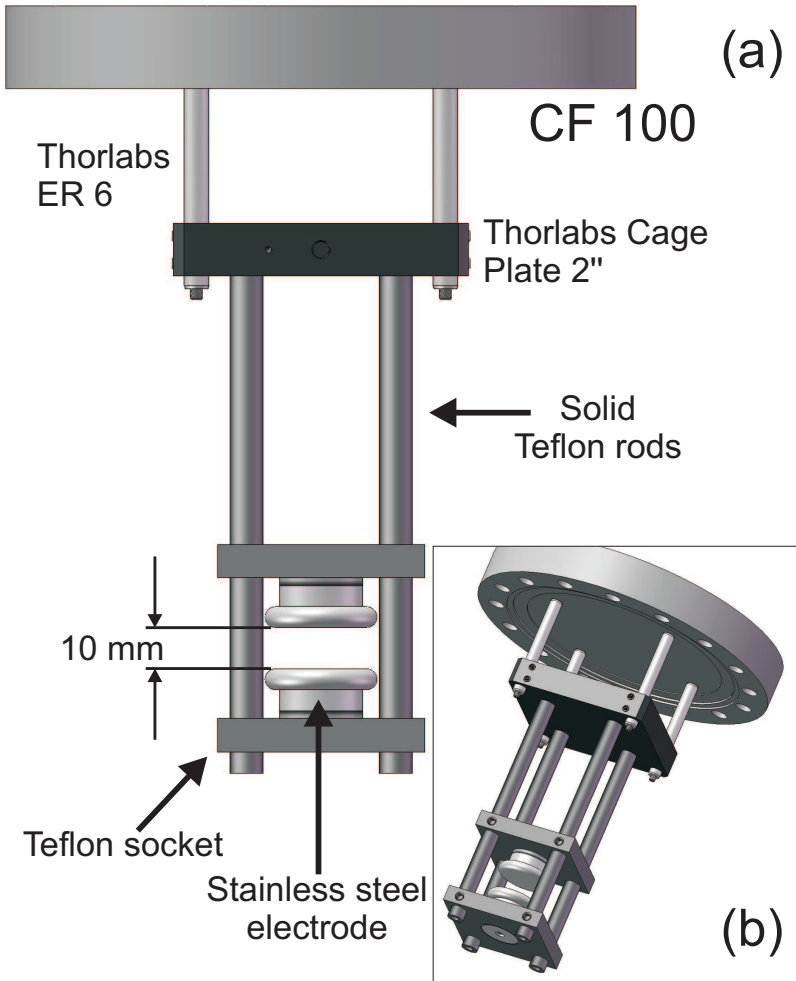


Figure 5.1.: True to scale model of the electric field plates suspended from a CF100 blind. In (a) the relevant parts are labelled. Teflon was used as insulator. The upper electrode is electrically connected to the CF100 flange, which is grounded. In inset (b) the screw thread of the lower electrode can be seen at the bottom of the picture. From this bottom side it is connected to an electrical feedthrough, which connects to the high voltage power supply.

5.3. Redesign of the lens system

When the vacuum chamber was constructed and built, both interaction zones were planned in the exact same way. After introduction of field plates, the lens system had to be changed, because the teflon construction does not allow to place the lens nearest to the fluorescence only 19 mm from the interaction zone (see Sec. 4.3). A bigger distance is required. Figure 5.2 shows the modified lens system. The second major change is that the direction of observation is now in opposition to the beam propagation ($-z$ -direction), because the field plates take already the y -direction of space, where the photomultiplier was looking in IZ1 (Figure 4.3). The third direction in space (x) is occupied by the laser beam for excitation. Further more the collecting mirror M is missing, which also halves the collected fluorescence. Beyond these changes only the lens distances have been changed. They were optimized with the WinLens package [Win06]. The principle is still a three lens system with two lenses inside vacuum (L4: $f_4 = 75$ mm and $f_5 = 100$ mm) and one lens outside ($f_6 = 150$ mm). The Lens L4 in Fig. 5.2 has a distance of 30 mm to the fluorescence spot.

Two disadvantages appear with the two major changes: firstly the photomultiplier detects infrared light from the oven nozzle now ($T = 840$ K); secondly the mirror is missing and the angle within which fluorescence light is collected, is smaller due to the bigger distance of the first lens (L4) to the fluorescence spot. The latter fact however is not that critical, because the volume in space where fluorescence appears is given by the laser diameter (2 mm) and the molecular beam spread 420 mm behind the collimation aperture (≈ 5 mm). This volume is covered by the lens system according to the optimization routine. But still a factor of two in fluorescence is missing.

The first steps with the second interaction zone included re-

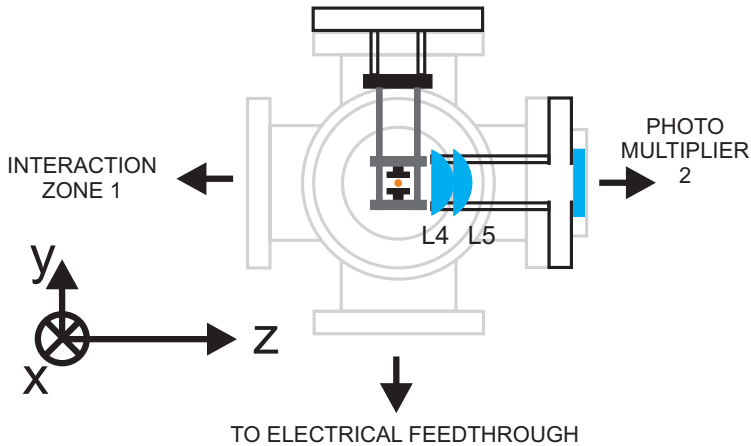


Figure 5.2.: Optical system in the second interaction zone (IZ2). The molecular beam propagates in z -direction. All three lenses are mounted using the Thorlabs two inch cage system. Two lenses are placed inside the vacuum, the third lens is not shown in this figure. Again the connection to the photomultiplier housing outside vacuum is self-built. Also not shown are the aperture rods in x -direction, which are fitted into the reducer flanges of IZ2 (Fig. 4.1) similarly to IZ1.

measuring some of the known lines from the excitation spectroscopy (Sec. 4.7 and Appendix A). The molecular signal was found immediately with the different photomultiplier model (Products For Research Inc., model R928, with appropriate housing). The higher background at PM2 due to the black body radiation of the oven nozzle could be reduced by means of a LINOS Calflex-X filter and use of lock-in technique. Signal-to-noise ratio allowed for studying the very weak low J lines at the bandhead, even with electric field (the Stark splitting with its intensity distributed on all M sub-components reduces the signal furthermore).

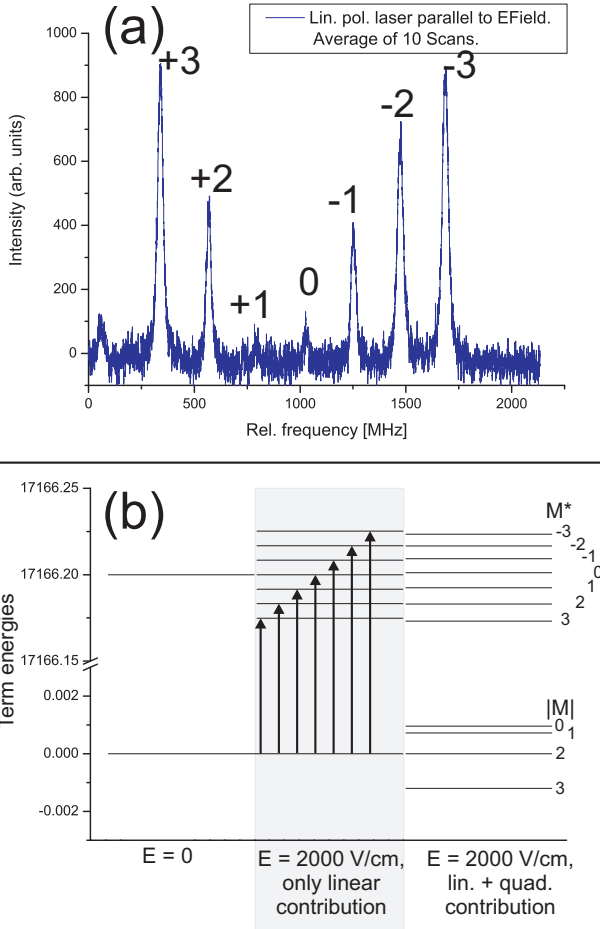


Figure 5.3.: (a) Example spectrum: π -excitation of the NaK B - X (3 - 0) Q(3) line showing mainly the linear Stark splitting of the $B^1\Pi$ state. Lines are named by M quantum number. (b) Underlying level scheme for the NaK B - X (3 - 0) Q(3), calculated with Eqs. (5.1), (5.2) and (5.3) and dipole moments from the calculation in Chapter 2.5. Note that the energy scale for the lower state is much smaller. Transitions are only plotted for the linear case, for $\Delta M = 0$ in the quadratic case it would also be easy to plot, for $\Delta M = \pm 1$ however (σ^\pm -excitation) the picture would get messy. Therefore this case is not given in this picture.

5.4. The Stark effect of NaK experimentally

The high voltage on the lower electrode is generated by a FUG HCN 350-35 000 power supply, which allows voltages up to 35 kV. Conditioning voltages did not go beyond 15 kV to avoid discharging which might damage the electrodes. The display on the device itself shows the applied voltage only with a precision of 0.1 kV, therefore a resistive voltage divider was implemented and calibrated. The voltage can now be determined with an uncertainty of ± 10 V, which gives at 2000 V a relative uncertainty of 0.5%.

Figure 5.3 shows a π -excitation of the NaK B-X (3-0) Q(3) line with a field strength of 2000 V/cm. As expected from the selection rule $\Delta M = 0$ that applies in this case, seven sub-components of the line can be seen. They seem to be equidistant, but from the intensities one can already guess, that some second order effect is present. Otherwise the pure $|M|^2$ dependence from the square of the Clebsch-Gordon coefficients that describe the relative intensity distribution would not be disturbed. Especially the appearance of $M = 0$ and the weakness of $M = +1$ is to be mentioned (see Fig. 5.3)

Figure 5.4 shows the case of laser polarization perpendicular to the direction of electric field lines which corresponds to σ^\pm -excitation and thus gives rise to $\Delta M = \pm 1$ transitions. Within this chapter the * shall denote the quantum numbers of the excited state, while symbols without star represent the ground state quantum numbers. The second order effect can be seen for higher values of the electric field as the components split into doublets except for $|M^*| = J^*$ and $|M^*| = 0$ (only one transition possible or degeneracy of both transitions). These small splittings in the spectra correspond directly to the term energy splitting in the ground state.

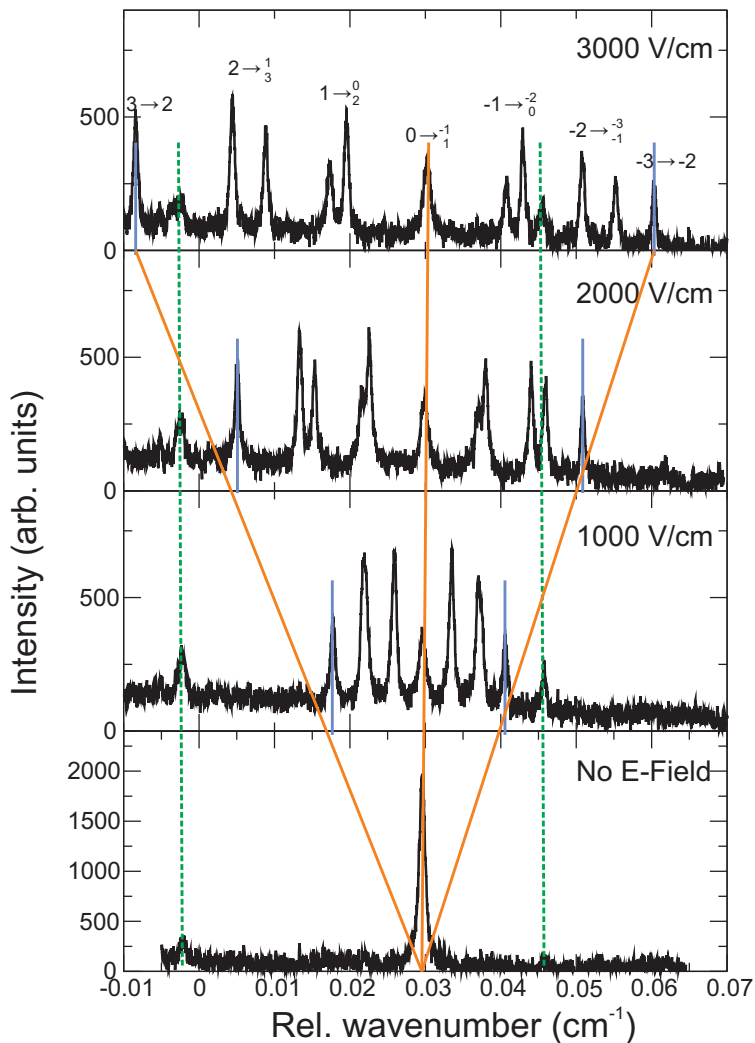


Figure 5.4.: Splitting of the NaK B-X (3-0) Q(3) line for several values of the electric field. For the $M^* = 0$ and $|M^*| = J$ solid are drawn to guide the eye. The dotted lines show underlying features that do not move or split with the electric field, probably high J molecular lines of a different band or lines from a homonuclear molecule. In the 3000 V/cm case quantum numbers in the form $M^* \rightarrow M$ display the $\Delta M = \pm 1$ selection rule for σ^\pm -excitation.

Lines in three different bands were measured: NaK B-X (3-0) Q(3) (several electric fields), NaK B-X (7-0) Q(4) with 2000 V/cm and NaK B-X (10-0) Q(2) and R(4), also with 2000 V/cm. The observation of the R-line checks for dipole moment of levels of opposite parity, namely e or f type of the state $B^1\Pi$.

It was a challenge to find lines with J as low as possible in order to not have too many components in the spectrum and too much reduced Stark effect by the large denominator in Eqs. (5.1), (5.2) and (5.3). In addition they should be well isolated to not complicate the evaluation by overlapping components from several lines which run through each other. These requirements were hard to fulfil, because the low J lines are usually at the bandhead, where the density of lines is high.

In Fig. 5.4 the zero component shows nearly no shift in frequency showing that $(\mu E)^2/B_v$ in both quadric expressions (5.2) and (5.3) are almost equal. Thus the two shifts almost cancel.

5.5. Evaluation of Stark spectra

Evaluation of the spectra was straight forward in calculating the term values for both states using the Eqs. (5.1), (5.2) and (5.3). The zero-field line at wavenumber F was then modified by the shifts in the following way (respecting the selection rules for the given polarization):

$$F' = F - f(J^*, M^*) \cdot (\mu^* E) + g(J^*, |M^*|^2) \cdot (\mu^* E)^2 - h(J, |M|^2) \cdot (\mu E)^2 \quad (5.5)$$

The $*$ denotes again the upper state quantities. The calculated (CALC) wavenumbers were compared to the observed ones (OBS) in the spectrum. As indicator for the goodness of fit the normal-

ized σ was calculated as follows:

$$\sigma = \sqrt{\frac{\sum_{i=1}^M (\frac{OBS-CALC}{\Delta OBS})^2}{N_{OBS}}} \quad (5.6)$$

where N_{OBS} is the number of measurements available and ΔOBS is the experimental uncertainty. Note that the denominator of the fraction does not subtract the number of degrees of freedom compared to the conventional definition of the standard deviation. The number of observations is too small to do these statistics. In order to compare the different model/fit approaches with the σ as indicator, it is better to define it the way above. A $\sigma = 1$ means that on average the differences between OBS and CALC are of the order of the given uncertainties of the observed lines of $\Delta OBS = 0.0001 \text{ cm}^{-1}$.

Now the dipole moments μ^* of the $B^1\Pi$ state and μ of the $X^1\Sigma^+$ state in expression (5.5) were varied and the pair with the smallest σ recognized as the best fit. Table 5.1 shows the final set of results (for now without uncertainties).

In all entries marked with \bullet , both dipole moments were varied for the fit. In the first line the ground state dipole moment $\mu = 2.49 \text{ D}$ is too small compared with the literature value of $2.73(9) \text{ D}$ [Wor81]. The reason is that no line splitting due the second order Stark effect in the ground state was resolved in the spectrum. The same is true for the NaK B-X (3-0) Q(3) 1000 V/cm recording (see Fig. 5.4) and for the NaK B-X (10-0) R(4) 2000 V/cm spectrum. For both components of a given M^* with $\Delta M = \pm 1$ the same wavenumber was set in the input file and a bigger uncertainty of 0.001 cm^{-1} was assigned to these transitions which explains the small σ values. Because the fit has no frequency splitting to determine μ , it tries to drag it somewhere in order to fit into the (broadened) component.

Transition NaK B-X	Electric field (V/cm)	μ^* (D)	μ_2^* (D)	μ (D)	σ	
(3-0) Q(3)	500	2.73		2.49	0.26	●
	500	2.73		2.73	0.26	○
	1000	2.72		2.75	0.19	●
	1500	2.72		2.68	0.29	●
	2000	2.73		2.72	0.66	●
	2500	2.74		2.73	0.70	●
	3000	2.75		2.74	1.71	●
	3000	2.75	2.73	2.74	1.69	③
(7-0) Q(4)	2000	2.56		2.67	0.46	●
(10-0) Q(2)	2000	2.36		2.75	2.78	●
	2000	2.36	2.35	2.75	2.78	③
(10-0) R(4)	2000	2.34		2.78	0.47	●

Table 5.1.: Fit results of the Stark evaluation. Uncertainties are not given in this table. Two parameter fits are marked by ● and ○, three parameter fits by ③. The cases where $\sigma > 1$ were not taken in the final evaluation, because we did not want to introduce additional errors. The dipole moment μ^* for $v^* = 10$ can be determined from the R line measurement, and in the case of 3000 V/cm for $v^* = 3$ enough other field values allow the determination of μ^* . These cases however have to be revisited to fully understand what happened. Until now it is unknown, if the fit is bad, or if errors occurred in the experimental spectrum or in the frequency axis construction.

For the Q(3) line 500 V/cm the fit was repeated with a fixed value of $\mu = 2.73$ D, the mean value from the other cases to keep internal consistency of the whole fit procedure (accidentally it is

the literature value). This case is marked with \circ and it can be seen, that there is no change of μ^* compared to before, which is also confirmed by a third approach, where no second order contributions were considered at all. This was done for all cases, where no line splitting was observed in the spectra. Only μ^* was varied and the fit is always good and bears the same μ^* as in the two parameter fits. This shows, that the second order contribution is not necessary to describe these spectra.

For higher field values σ increases (especially in the case of 3000 V/cm), and we tried to model this by polarization effects. These fits are marked with the symbol $\textcircled{3}$ in the table. The first and simple approach was to not use the same μ^* in the linear and quadratic terms of expression (5.5), but to write instead

$$F' = F - f(J^*, M^*) \cdot (\mu^* E) + g(J^*, |M^*|^2) \cdot (\mu_2^* E)^2 - h(J, |M|^2) \cdot (\mu E)^2 \quad (5.7)$$

which effectively includes polarization effects. The corresponding μ_2^* of the three-parameter fit can be found in the 4th column of Table 5.1. Unfortunately, the quality of the fit did not improve by this procedure, the M^* -dependence does not differ too much between second order energy for the dipole moment and the polarizability for expecting an improvement by introducing the correct J and M^2 dependence for the case $\Lambda \neq 0$, different than in Eq. (5.4). Also a detailed look into the spectra did not reveal some readout errors in the experimental spectra or a single line dropping out of the fit. These fit results are therefore not considered in the calculation for the present. The fit with a σ greater than one introduces additional uncertainties for the derived quantity μ^* . Clearly these spectra have to be revisited carefully and the model has to be refined for higher fields to fully understand the structure.

5.6. Uncertainty budget

According to Eq. (5.5) (μE) and ($\mu^* E$) are the primarily determined quantities in the measurements, because its uncertainty is directly connected with the uncertainty in determination of line position of 0.0001 cm^{-1} (3 MHz). With a $\sigma = 1$ one can assume that on average this absolute uncertainty is justified. The relative uncertainty for $\mu^* E$ is smaller than for μE , because the span of the complete structure is bigger (1-2 GHz) than the splitting that determines the ground state dipole moment (up to 250 MHz). The relative uncertainty is therefore $2 \cdot 10^{-3}$ for $\mu_v^* E$ and $2 \cdot 10^{-2}$ for $\mu_v E$ (in the fits where $(\mu_v E)^2$ is determined).

Of course, it is not satisfying to stay with the product of $\mu_v E$ or $\mu_v^* E$ and one has to care about an error estimation on the electric field. The first approach is to take the relative uncertainties of distance and voltage determination being $5 \cdot 10^{-3}$ in both cases (Sec. 5.2 and 5.4), which will add up to an uncertainty in electric field strength of $7 \cdot 10^{-3}$. For taking full advantage of the accuracy of $\mu_v^* E$ for the determination of μ_v^* one has to calibrate the field to a better standard.

We assume that the field does not change with time due to the rigid construction of the electrode setup. Experimentally a change of applied voltage was not observed with the resistive voltage divider and the control deviation of the power supply is $< 1 \cdot 10^{-4}$ [HCN97].

The following list contains possible different sources of uncertainty that should be considered, but it is estimated that their respective uncertainties are smaller than the limit given above:

- *Contact potentials*: due to a not symmetric setup of electrical connections a residual contact voltage could result in a charging of the electrodes (no closed loop). These voltages

can reach several volts, compared to the voltages applied in the experiment, the relative error will clearly be below 1%.

- *Thermal expansion due to radiative heating:* The hot oven nozzle could heat the electrode setup radiatively, which would lead to a different plate separation. Considering the typical thermal expansion coefficient of 10^{-5} K^{-1} , we would need to heat up the electrode array by 100 K (which is unrealistic) to get a significant contribution in the uncertainty budget.
- *Charging effects:* The beam always contains ions in addition to atoms and molecules, which could lead to sticking a net charge, that influences the electric field strength. But this influence is probably negligible observing the beam density at the position of the electrodes. Density of the beam is very small, because the amount of material that can be traced on the end windows or on lens L4 in Fig. 5.2 is in the μm range after two years of beam operation.
- *Deposition of material,* which leads to a different electrode distance is already covered by the last argument.

The main part in uncertainty is coming from geometry and voltage measurement as described above. The M subcomponents in the spectra do not show asymmetry or broadening, a fact which indicates a good homogeneity of the field.

5.7. Results and comparison with *ab initio* data

The values for the dipole moments in Table 5.1 were determined by dividing the product μE from the fit by the electric field strength. Uncertainties are not given in the table, because the

purpose was to show the trend of the numbers with the different fit approaches. Two things can be noted already from this table:

1. The dipole moment μ^* of the $B^1\Pi$ state in the 3^{rd} column decreases with increasing v as predicted by theory (see Fig. 2.5)
2. The dipole moment μ of the $X^1\Sigma^+$ state in the 5^{th} column is in agreement with the value of $\mu = 2.73(9)$ within its error limits reported by Wormsbecher in [Wor81].

Relative uncertainties for the ground and excited state dipole moments are derived from the squared sums of relative uncertainties of electric field strength and the respective products $(\mu_v E)$ or $(\mu_v^* E)$. The square root of this sum is the relative uncertainty given in Table 5.2, where the values for the three different vibrational states are listed (the value for $v^* = 3$ is an average of the measurements for different electric fields).

A second approach to calculate the dipole moments is to rescale the electric field using the value of the ground state dipole moment that is reported in the literature: $\mu_{Lit} = 2.73(9)$ [Wor81]. The mean value of the ground state product that is determined in this study corresponds to the literature value of the dipole moment times an electric field that can be determined as follows:

$$E = \frac{(\mu E)_{OBS}}{\mu_{Lit}}. \quad (5.8)$$

The uncertainty of this electric field is now determined by the uncertainty of the literature value in the denominator $3.3 \cdot 10^{-2}$ and the uncertainty of the product $2 \cdot 10^{-2}$ for the ground state splitting. By dividing the upper state product $(\mu_v^* E)$ by the rescaled electric field one obtains a second set of dipole moments with different uncertainties, which are actually higher than the

Dipole moments B ¹ Π state				
v^*	This work (μ_{exp}^*)	Ab initio (μ_{ai}^*)	Ratio μ_{ai}^*/μ_{exp}^*	
3	2.73(2) D	2.73(11) D*	3.12 D	1.13
7	2.56(2) D	2.56(10) D*	2.87 D	1.12
10	2.34(2) D	2.34(9) D*	2.62 D	1.11
Dipole moment X ¹ Σ ⁺ state				
v	This work	[Wor81]	Ab initio (μ_{ai})	Ratio μ_{ai}/μ_{exp}
0	2.73(6) D	2.73(9) D	2.78 D	1.02

Table 5.2.: Comparison of the dipole moments from *ab initio* data with the experimental values from this study. A constant scaling factor can map the theoretical data to the experimental values. Number marked with * are obtained by calibrating the field with the dipole given in [Wor81].

ones determined with by simple division because of the uncertainty of the literature value. Accidentally the mean dipole moment μ of the ground state $v = 0$ level is the same as the literature value. Therefore the second approach yields the same numbers as before but with bigger uncertainty. These errors are given in Table 5.2 as a second value marked by the * symbol.

Figure 5.5 shows a graphical representation of what is printed in Table 5.2: The circles display the full *ab initio* curve (compare Fig. 2.5) and the squares the experimental data with their uncertainties. By applying a scaling factor of $A_{scale} = 1.12$ (the mean of the three factors in Table 5.2) to the theoretical values, one can map the curves onto each other. An error of 12 % for a theoretical calculation of an excited state is a very good result. For the ground state dipole moment μ one can also calculate this ratio with $\mu_{ai} = 2.78$ to be $\mu_{ai}/\mu_{exp} = 1.02$, which indicates that the

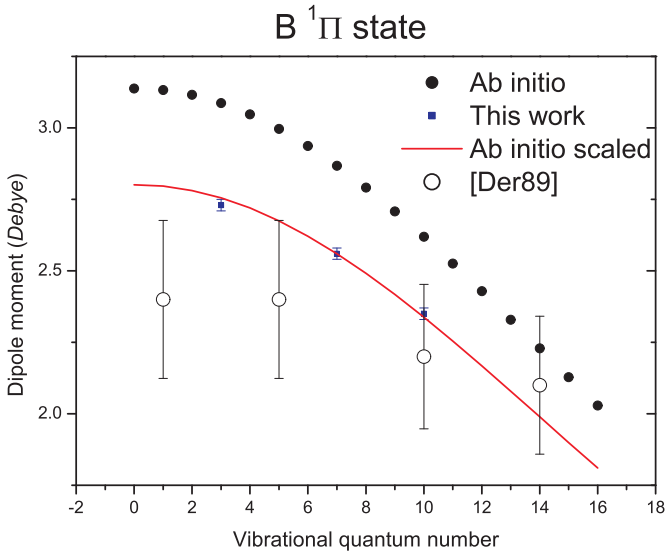


Figure 5.5.: Comparison of the experimental data (squares) with the *ab initio* calculation (filled circles). The solid line shows the calculated values scaled by a factor of $A_{scale} = 1.12$. The potential used to get the v dependence of the *ab initio* dipole moment function is from Katô [Kat90]. Open circles with uncertainties are the experimental results from [Der89].

calculation for the ground state yields even more precise values.

Also given in Fig. 5.5 are other experimental results from the work of Derouard *et al.* [Der89]. They determined μ^* for the B ¹Π state for $v = 1, 5, 10$ and 14 with a total uncertainty of 11.5 % using electric field induced $e - f$ mixing spectroscopy. For $v = 10$ our μ^* value lies within the error bar of the other measurement. For lower v values these measurements do not reflect the simple scaling of the *ab initio* values any more.

CONCLUSION & OUTLOOK

This thesis was concerned with the experimental and theoretical exploration of alkali dimers in various aspects. Although the title focusses on dipole moments, the preparatory work, before measuring the desired quantity, covers spectroscopy of energy levels to gain information about potential energy curves and cold collision properties. Also the theoretical part verifies its calculation first by comparing the potential energy curves with other calculations or experimental data, before focussing on the dipole moment functions.

The work includes an introduction into quantum chemistry, some improvements on the code and verification at the examples of Rb_2 and Cs_2 , before the dipole moment function of NaK is described as function of internuclear distance and converted into a vibrational dependence.

Experimentally a pre-study on the NaK dimer enabled the beam spectroscopy on the newly built apparatus. The theoretical dipole moment prediction made it possible to estimate energy splittings

and to design the beam experiment to the necessary precision to allow for detection of the small shifts given by the second order Stark effect of the ground state.

The beam spectroscopy allowed to determine the upper state dipole moment μ^* with a relative uncertainty of $7 \cdot 10^{-3}$, the ground state dipole moment for $v = 0$ with an relative uncertainty of $2 \cdot 10^{-2}$. The very high precision in frequency/wavenumber measurement of ± 3 MHz would even allow for a smaller uncertainty when the electric field would be calibrated to a better standard.

Dipole moments for the excited $B^1\Pi$ state were measured for several vibrational levels. The result shows the quality of the quantum chemistry calculation for the excited state giving only a deviation of 12% for the dipole (compare Fig. 5.5).

Continuation on dipole moments for the B state

The next consequential step will definitely be an experiment to extend these measurements in order to map the dipole moment function more completely. At least one more data point at lower v is necessary to verify the saturation behaviour. For higher v points are needed to indeed prove the further decrease in dipole moment as predicted by the quantum chemistry calculation. The laser equipment definitely allows to cover the whole v range as shown by the systematic excitation spectroscopy (Appendix A). For higher v quantum numbers perturbations have to be taken into account. More measurements in the excited state will also show, if the simple scaling factor that is introduced in Chapter 5.7 is sufficient or if a more elaborate function is needed to map the theoretical calculation to the experimental data.

Dipole moments for the ground state

The ground state could be explored in the same way, i.e. measuring the vibrational dependence of the ground state dipole moment; the chamber is suited for that in terms of high resolution and precision. The *ab initio* calculation also provides these data (see Fig. 2.5). The recommendation would then be to use higher field strengths to reduce the relative error in frequency determination for the ground state product (μE). Of course one has to populate the appropriate levels one wants to measure, because in the molecular beam mainly the $v = 0$ state is populated (Sec. 4.4).

Such an experiment is definitely more complex to handle, because at least two lasers have to be used. There were some attempts with STIRAP [Ber98] in the scope of this thesis to prepare high vibrational levels in the ground state, which were abandoned after realizing that the scanning laser might have a too broad line width to create a good adiabatic passage. But a transfer to higher v in the ground state can also be done by Franck-Condon pumping (see Fig. 6.1 at the example of K_2 : the pumping laser L1 drives a transition that populates various vibrational levels of the X state according to the corresponding Franck-Condon factors). One only pumps about 10% of the molecules, but needs just to provide one more laser to populate the level of interest instead of two. From the target level in the ground state the spectroscopy works the same way as before from $v = 0$.

Sign of the dipole moments

One highly interesting point in measuring dipole moments will be the determination of the sign (for ground state and for excited state) to compare with the theoretical prediction. With the

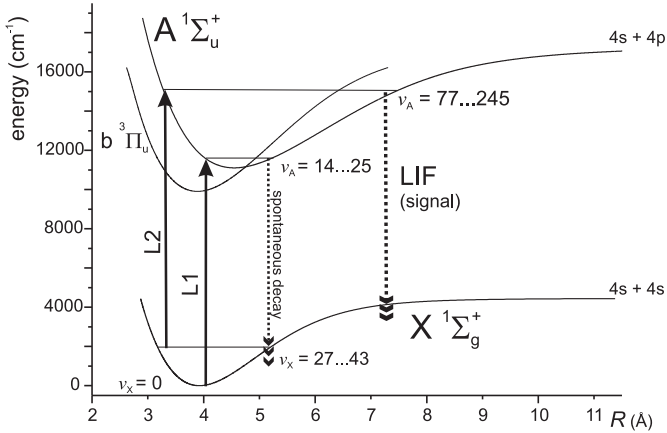


Figure 6.1.: Simplified potential scheme of K_2 . Initially, the molecules are in the vibrational ground state of the $X^1\Sigma_g^+$ state. The first laser L1 drives Franck-Condon pumping. The spectroscopy is done with a second laser L2. Reprinted from [Fal06a].

applied excitation in the experiment perpendicular to the electric field it was only possible to excite σ^\pm at the same time. To selectively excite only one circular polarization one would have to shine in the laser light in direction of the electric field. This can be accomplished either by using transparent electrodes (glass substrates with semi transparent metal layers) or by giving an angle of the excitation laser beam which creates a projection into electric field direction. The latter approach was not feasible in the current experimental setup because the aperture rods do not allow for such an angle right now.

Spectroscopy up to the dissociation limit of the ground state

STIRAP or Franck-Condon pumping could also be applied to investigate the long-range parts of the potential curves. With the $B^1\Pi$ state data from Kasahara [Kas91] (or the $A^1\Sigma^+$ state potential description from Ross [Ros88]) one could plan experiments similar to the beam spectroscopy for Na_2 [Sam03] or K_2 [Fal06a] performed in our group (see also Fig. 6.1). Measuring energy levels up to the dissociation limit aims for a more precise description of cold collision properties. In this way the data that were collected in the heatpipe study (Chapter 3 or [Ger08]) could be refined. A beam apparatus is specially suited for such experiments because the preparation step can be spatially separated from the detection by using both interaction zones.

De-perturbation of the excited state(s)

Further more the data gained with the excitation spectroscopy that are already assigned (see Appendix A) could be either extended, or put into a frame with the kindly provided original data from S. Kasahara [Kas09]. Such accumulation of data from different groups to perform a combined fit on them was already successfully performed in molecular spectroscopy. A global de-perturbation analysis of the $[B^1\Pi, c^3\Sigma^+]$ (compare e.g. [Doc07a, Doc07b] for NaRb or [Sal09] for the $[A^1\Sigma_u^+, b^3\Pi_u]$ system of Rb_2) would be a fruitful outcome of the data from the beam measurements that turned out to be so useful already for the Stark measurements.

Change of oven-concept

During the testing and work with the used oven concept that heats the container from outside the vacuum chamber, several

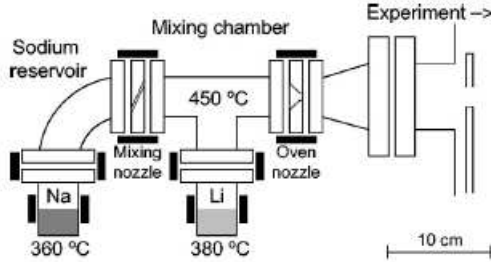


Figure 6.2.: The next generation oven concept with separated reservoirs for different species and nozzle with separate heating, here shown for the example of Na and Li. Reprinted from [Sta05].

annoying drawbacks were recognized (see Chapter 4.8). Therefore new parts were ordered and constructed to build up an enhanced beam source following the idea of Stan and Ketterle [Sta05] to use only standard vacuum parts to build the source, which makes it cheap, easy to assemble and some parts easy replaceable. Fig. 6.2 shows the setup, which we adopted entirely.

Only the heating of the assembly, two shells with drill holes that will carry the cartridge heaters, was constructed newly and manufactured in the institute workshop. This oven will allow to set separated temperatures and thus vapour pressures for two different atomic species and has a nozzle, that can be heated separately. The cartridge heaters are still accessible from outside vacuum, which makes the heaters very easy accessible and simplifies the setup, Even cooling shields inside vacuum are planned to improve the beam condition and minimize the load for the vacuum pumps in the oven part of the chamber [Knö09].

Final remark

The above fields of research might give a glimpse how powerful a machine like the newly built beam apparatus is. It opens a variety of possible research directions that one can go for in the future.

The new oven concept with two containers will allow to investigate other heteronuclear species. The two species BEC experiments that were mentioned in the Introduction are focussing on the ground states, where dipole moments were determined [Ni08]. A comparison with these measurements is of great interest.

TRANSITION FREQUENCIES B – X

Here the transition frequencies of NaK $B^1\Pi \leftarrow X^1\Sigma^+$ are listed. All energies are given in cm^{-1} . The relative uncertainty (for line differences) within a single scan is 0.0001 cm^{-1} . The iodine trace for absolute calibration only allows for an uncertainty of 0.001 cm^{-1} . Since it is not marked here, for which transitions the difference is known with a smaller uncertainty, the reader has to assume the uncertainty of 0.001 cm^{-1} for every line. This is precise enough to find the lines with a wavemeter like the WS7. The full information is available in electronic form. Some bands are missing in the collection:

- The 0 – 0 band was not recorded.
- The 4 – 0 and 8 – 0 bands were recorded but not assigned due to perturbations.
- The 12 – 0 band was recorded, but not processed, because the reference trace information has to be treated more carefully in order to construct the frequency axes for the scans.

B - X 1 - 0 band

R 0	17035.5414				
R 1	17035.6335	Q 1	17035.3518		
R 2	17035.6770	Q 2	17035.2540	P 2	17034.9722
R 3	17035.6716	Q 3	17035.1079	P 3	17034.6849
R 4	17035.6175	Q 4	17034.9129	P 4	17034.3478
R 5	17035.5148	Q 5	17034.6690	P 5	17033.9635
R 6	17035.3630	Q 6	17034.3753	P 6	17033.5305
R 7	17035.1625	Q 7	17034.0344	P 7	17033.0462
R 8	17034.9129	Q 8	17033.6446	P 8	17032.5146
R 9	17034.6148	Q 9	17033.2036	P 9	17031.9331
R10	17034.2664	Q10	17032.7153	P10	17031.3034
R11	17033.8707	Q11		P11	17030.6262
R12	17033.4237	Q12	17031.5923	P12	17029.8996
R13	17032.9287	Q13	17030.9561	P13	17029.1229
R14	17032.3861	Q14	17030.2726	P14	17028.2987
R15	17031.7926	Q15	17029.5386	P15	17027.4255

B - X 2 - 0 band

R 0	17102.3069				
R 1	17102.3851	Q 1	17102.1064		
R 2	17102.4210	Q 2	17102.0042	P 2	17101.7272
R 3	17102.4059	Q 3	17101.8505	P 3	17101.4346
R 4	17102.3397	Q 4	17101.6452	P 4	17101.0915
R 5	17102.2219	Q 5	17101.3894	P 5	17100.6967
R 6	17102.0517	Q 6	17101.0826	P 6	17100.2505
R 7	17101.8316	Q 7	17100.7232	P 7	17099.7527
R 8	17101.5594	Q 8	17100.3133	P 8	17099.2036
R 9	17101.2361	Q 9	17099.8510	P 9	17098.6031

R10	17100.8612	Q10	17099.3374	P10	17097.9519
R11	17100.4358	Q11	17098.7729	P11	17097.2484
R12	17099.9573	Q12	17098.1570	P12	17096.4946
R13	17099.4278	Q13	17097.4889	P13	17095.6886
R14	17098.8465	Q14	17096.7714	P14	17094.8324
R15	17098.2135	Q15	17096.0004	P15	17093.9229

B – X **3 – 0** band

R 0	17166.6587				
R 1	17166.7408	Q 1	17166.4679		
R 2	17166.7695	Q 2	17166.3605	P 2	17166.0888
R 3	17166.7440	Q 3	17166.1997	P 3	17165.7910
R 4	17166.6651	Q 4	17165.9838	P 4	17165.4392
R 5	17166.5308	Q 5	17165.7152	P 5	17165.0349
R 6	17166.3443	Q 6	17165.3920	P 6	17164.5756
R 7	17166.1037	Q 7	17165.0159	P 7	17164.0625
R 8	17165.8089	Q 8	17164.5847	P 8	17163.4945
R 9	17165.4594	Q 9	17164.0998	P 9	17162.8729
R10	17165.0575	Q10	17163.5601	P10	17162.2000
R11	17164.6003	Q11	17162.9685	P11	17161.4718
R12	17164.0890	Q12	17162.3222	P12	17160.6894
R13	17163.5225	Q13	17161.6203	P13	17159.8540
R14	17162.9022	Q14	17160.8658	P14	17158.9630
R15	17162.2297	Q15	17160.0574	P15	17158.0185

B – X **5 – 0** band

R 0	17288.2313				
R 1	17288.3030	Q 1	17288.0409		
R 2	17288.3156	Q 2	17287.9220	P 2	17287.6603

R 3	17288.2689	Q 3	17287.7454	P 3	17287.3527
R 4	17288.1634	Q 4	17287.5083	P 4	17286.9839
R 5	17287.9972	Q 5	17287.2135	P 5	17286.5588
R 6	17287.7737	Q 6	17286.8561	P 6	17286.0745
R 7	17287.4896	Q 7	17286.4443	P 7	17285.5270
R 8	17287.1455	Q 8	17285.9723	P 8	17284.9229
R 9	17286.7433	Q 9	17285.4373	P 9	17284.2639
R10	17286.2844	Q10	17284.8448	P10	17283.5390
R11	17285.7646	Q11	17284.1979	P11	17282.7572
R12	17285.1819	Q12	17283.4851	P12	17281.9149
R13	17284.6127	Q13	17282.7144	P13	17281.0185
R14	17283.8426	Q14	17281.8841	P14	17280.0556
R15	17283.0848	Q15	17280.9990	P15	17279.0381

$B - X$ **6 - 0** band

R 0	17345.4758				
R 1	17345.5416	Q 1	17345.2823		
R 2	17345.5453	Q 2	17345.1590	P 2	17344.9033
R 3	17345.4886	Q 3	17344.9736	P 3	17344.5911
R 4	17345.3694	Q 4	17344.7278	P 4	17344.2165
R 5	17345.1850	Q 5	17344.4191	P 5	17343.7772
R 6	17344.9420	Q 6	17344.0461	P 6	17343.2778
R 7	17344.6384	Q 7	17343.6138	P 7	17342.7173
R 8	17344.2723	Q 8	17343.1185	P 8	17342.0946
R 9	17343.8408	Q 9	17342.5619	P 9	17341.4094
R10	17343.3490	Q10	17341.9433	P10	17340.6619
R11	17342.7958	Q11	17341.2615	P11	17339.8530
R12	17342.1804	Q12	17340.5176	P12	17338.9829
R13	17341.5016	Q13	17339.7121	P13	17338.0480
R14	17340.7605	Q14	17338.8451	P14	17337.0547

R15	17339.9575	Q15	17337.9134	P15	17335.9956
-----	------------	-----	------------	-----	------------

B – X **7** – **0** band

R 0	17400.3986				
R 1	17400.4591	Q 1	17400.2099		
R 2	17400.4551	Q 2	17400.0809	P 2	17399.8306
R 3	17400.3867	Q 3	17399.8813	P 3	17399.5097
R 4	17400.2535	Q 4	17399.6266	P 4	17399.1249
R 5	17400.0565	Q 5	17399.3026	P 5	17398.6764
R 6	17399.7938	Q 6	17398.9154	P 6	17398.1636
R 7	17399.4631	Q 7	17398.4624	P 7	17397.5857
R 8	17399.0712	Q 8	17397.9452	P 8	17396.9436
R 9	17398.6135	Q 9	17397.3626	P 9	17396.2341
R10	17398.0916	Q10	17396.7157	P10	17395.4637
R11	17397.5032	Q11	17396.0022	P11	17394.6254
R12	17396.8513	Q12	17395.2260	P12	17393.7240
R13	17396.1318	Q13	17394.3823	P13	17392.7568
R14	17395.3494	Q14	17393.4752	P14	17391.7236
R15	17394.4993	Q15	17392.5016	P15	17390.6282

B – X **9** – **0** band

R 0	17503.5801				
R 1	17503.6039	Q 1	17503.3731		
R 2	17503.6274	Q 2	17503.2486	P 2	17502.0115
R 3	17503.5094	Q 3	17503.0352	P 3	17502.6776
R 4	17503.3447	Q 4	17502.7505	P 4	17502.2736
R 5	17503.1090	Q 5	17502.3947	P 5	17501.8000
R 6	17502.8015	Q 6	17501.9700	P 6	17501.2546
R 7	17502.4236	Q 7	17501.4817	P 7	17500.6378

R 8	17501.9778	Q 8	17500.9079	P 8	17499.9530
R 9	17501.4735	Q 9	17500.2703	P 9	17499.1969
R10	17500.8735	Q10	17499.5633	P10	17498.3699
R11	17500.2138	Q11	17498.7854	P11	17497.4718
R12	17499.4857	Q12	17497.9365	P12	17496.5053
R13	17498.6863	Q13	17497.0190	P13	17495.4664
R14	17497.8157	Q14	17496.0301	P14	17494.3604
R15	17496.8751	Q15	17494.9708	P15	17493.1824

$B - X$ 10 - 0 band

R 0	17551.7725				
R 1	17551.8063	Q 1	17551.6027		
R 2	17551.7921	Q 2	17551.4554	P 2	17551.2221
R 3	17551.7037	Q 3	17551.2364	P 3	17550.8841
R 4	17551.5279	Q 4	17550.9438	P 4	17550.4747
R 5	17551.2638	Q 5	17550.5769	P 5	17549.9931
R 6	17550.9560	Q 6	17550.1375	P 6	17549.4365
R 7	17550.5575	Q 7	17549.6244	P 7	17548.8083
R 8	17550.0893	Q 8	17549.0390	P 8	17548.1058
R 9	17549.5459	Q 9	17548.3796	P 9	17547.3295
R10	17548.9301	Q10	17547.6467	P10	17546.4811
R11	17548.2402	Q11	17546.8408	P11	17545.5579
R12	17547.4760	Q12	17545.9611	P12	17544.5635
R13	17546.6390	Q13	17545.0085	P13	17543.4931
R14	17545.7273	Q14	17543.9811	P14	17542.3502
R15	17544.7435	Q15	17542.8808	P15	17541.1349

 B – X **11 – 0** band

R 0	17597.9563				
R 1	17597.9808	Q 1	17597.7531		
R 2	17597.9421	Q 2	17597.6006	P 2	17597.3715
R 3	17597.8279	Q 3	17597.3706	P 3	17597.0306
R 4	17597.6369	Q 4	17597.0677	P 4	17596.6126
R 5	17597.3695	Q 5	17596.6876	P 5	17596.1203
R 6	17597.0272	Q 6	17596.2329	P 6	17595.5466
R 7	17596.6086	Q 7	17595.6974	P 7	17594.9005
R 8	17596.1144	Q 8	17595.0894	P 8	17594.1784
R 9	17595.5392	Q 9	17594.4023	P 9	17593.3791
R10	17594.8907	Q10	17593.6404	P10	17592.5035
R11	17594.1657	Q11	17592.8014	P11	17591.5519
R12	17593.3637	Q12	17591.8871	P12	17590.5237
R13	17592.4845	Q13	17590.8963	P13	17589.4191
R14	17591.5285	Q14	17589.8262	P14	17588.2372
R15	17590.4950	Q15	17588.6806	P15	17586.9794

 B – X **13 – 0** band

R 0	17684.3264				
R 1	17684.3575	Q 1	17684.1140		
R 2	17684.2996	Q 2	17683.9785	P 2	17683.7313
R 3	17684.1429	Q 3	17683.7086	P 3	17683.4065
R 4	17683.9379	Q 4	17683.3988	P 4	17682.9685
R 5	17683.6334	Q 5	17682.9864	P 5	17682.4498
R 6	17683.2438	Q 6	17682.4934	P 6	17681.8472
R 7	17682.7752	Q 7	17681.9165	P 7	17681.1624
R 8	17682.2238	Q 8	17681.2572	P 8	17680.3949
R 9	17681.5901	Q 9	17680.5162	P 9	17679.5464

R10	17680.8746	Q10	17679.6924	P10	17678.6151
R11	17680.0777	Q11	17678.7869	P11	17677.6015
R12	17679.1977	Q12	17677.7991	P12	17676.5009
R13	17678.2367	Q13	17676.7306	P13	17675.3317
R14	17677.1926	Q14	17675.5801	P14	17674.0732
R15	17676.0655	Q15	17674.3467	P15	17672.7325

$B - X$ **14 - 0** band

R 0	17724.4879				
R 1	17724.5084	Q 1	17724.2986		
R 2	17724.4443	Q 2	17724.1294	P 2	17723.9192
R 3	17724.2951	Q 3	17723.8755	P 3	17723.5603
R 4	17724.0619	Q 4	17723.5356	P 4	17723.1157
R 5	17723.7433	Q 5	17723.1131	P 5	17722.5864
R 6	17723.3389	Q 6	17722.6039	P 6	17721.9720
R 7	17722.8514	Q 7	17722.0099	P 7	17721.2737
R 8	17722.2773	Q 8	17721.3311		
R 9	17721.6190				
R10	17720.8736				

$B - X$ **15 - 0** band

		Q 1	17762.7268		
R 2	17762.8738	Q 2	17762.5676		
R 3	17762.7135	Q 3	17762.3044		
R 4	17762.4647	Q 4	17761.9548	P 4	17761.5434
R 5	17762.1295	Q 5	17761.5155		
R 6	17761.7042	Q 6	17760.9898	P 6	17759.3758
R 7	17761.1922	Q 7	17759.3785	P 7	17759.6585
R 8	17760.5942	Q 8	17759.6756	P 8	17758.8555

R 9	17759.9067	Q 9	17758.8889	P 9	17757.9655
R10	17759.1316	Q10	17758.0124	P10	17756.9852
R11	17758.2681	Q11	17757.0463	P11	17755.9171
R12	17757.3147	Q12	17755.9931	P12	17754.7633
R13	17756.2738	Q13	17755.8539	P13	17753.5205
R14	17755.1481	Q14	17753.6252		
R15	17753.9315			P15	17750.7706

COHERENT DYE LASERS

B.1. Dye laser recipes

Rhodamine 6G

1 g	Rhodamine 6G	5 min ultrasonic bath
50 ml	Methanol	
+ 1.5 l	Ethylene glycol	

Rhodamine 110

1 g	Rhodamine 110	5 + 5 min ultrasonic bath
80 ml	Methanol	
+ 1.5 l	Ethylene glycol	

DCM

2 g	DCM	5 + 5 min ultrasonic bath
100 ml	Methanol	
<hr/>		
+ 1.5 l	Ethylene glycol	
<hr/>		

Coumarine 334

750 mg	Coumarine 334	5 + 5 min ultrasonic bath
75 ml	Methanol	
<hr/>		
+ 1.5 l	Ethylene glycol	
<hr/>		

B.2. Adjustment of a Lyot filter

The lyot filter for the ring laser (Graz design) can be adjusted in order to maximize power for a certain wavelength or to enable maximum tunability for the laser. This is the adjustment procedure for maximum tunability:

1. One starts with only the middle plate (the thinnest one) and brings the laser to oscillation. The maximum of transmission should be at about 45 angle. Note the wavelength / wavenumber of this position.
2. The next thicker plate is installed now. Bring the laser to oscillation and adjust the angle of the second plate relative to the first one in such a way, that the transmission maximum is again at the wavelength noted in the step before. The difference in angle of both plates should not be bigger than 10.
3. Install the third plate and bring the laser to operation again. This last installed plate should now be as parallel (in angle) as possible to the plate built in before. Fine adjustment can be done with the laser operating.

LIST OF FIGURES

2.1.	Graphical illustration of HF-procedure	18
2.2.	Chain of programs in AUTOCHIP	20
2.3.	Jumps in asymptotes in the Rb dimer	24
2.4.	Long range behaviour of <i>ab initio</i> curves	26
2.5.	Permanent electric dipole moments for NaK	30
3.1.	Heatpipe excitation scheme	35
3.2.	LIF setup	36
3.3.	Heatpipe example spectrum	41
3.4.	Observed quantum numbers used in the analysis	42
3.5.	Comparison of ground state potential energy curves	47
4.1.	Molecular beam setup	58
4.2.	Oven construction	60
4.3.	Optics setup for first interaction zone	62
4.4.	Rotational temperature (potassium dimer)	64
4.5.	Beam velocity measurement	66
4.6.	The first complete bandhead	68
5.1.	Electric field plates	77

5.2. Lens system in second interaction zone	79
5.3. NaK B - X (3 - 0) Q(3) π -excitation	80
5.4. NaK B - X (3 - 0) Q(3) σ^\pm -excitation	82
5.5. Comparison of dipole moments	91
6.1. FC-pumping scheme for K_2	96
6.2. Next generation oven concept	98

LIST OF TABLES

1.1.	Atomic unit conversion	7
1.2.	Typical quantities in atomic units	8
2.1.	The low order GTOs	16
2.2.	Results of C_4 fit	28
3.1.	Excitation paths in heatpipe study	38
3.2.	Parameters of the analytic representation of the potential energy curve for the $X^1\Sigma^+$ state of NaK. . .	43
3.3.	Parameters for the $X^1\Sigma^+$ state of NaK. (Continuation of Table 3.2.)	45
3.4.	Parameters of the analytic representation of the potential energy curve for the $a^3\Sigma^+$ state of NaK. . .	46
3.5.	Comparison of potential parameters	49
3.6.	Dunham-type coefficients for the $a^3\Sigma^+$ state of NaK	51
3.7.	Scattering lengths for the $X^1\Sigma^+$ and $a^3\Sigma^+$ molecular states of NaK	53
5.1.	Fit results of the Stark evaluation	85
5.2.	NaK: v -dependent dipole moments	90

BIBLIOGRAPHY

- [All04] O. Allard
Long-range interactions in the Calcium dimer studied by molecular spectroscopy
Ph.D. thesis, IQO Hannover (2004)
- [Ami02] C. Amiot and O. Dulieu
J. Chem. Phys. **117**(11) 5155–5164 (2002)
DOI: [10.1063/1.1499122](https://doi.org/10.1063/1.1499122)
- [Aym05] M. Aymar and O. Dulieu
J. Chem. Phys. **122**(20) 204302 (2005)
DOI: [10.1063/1.1903944](https://doi.org/10.1063/1.1903944)
- [Aym07] M. Aymar and O. Dulieu
Mol. Phys. **105**(11) 1733–1742 (2007)
DOI: [10.1080/00268970701494016](https://doi.org/10.1080/00268970701494016)
- [Aym09] M. Aymar, N. Bouloufa, J. Deiglmayr, A. Gerdes and
O. Dulieu
J. Chem. Phys.
To be published
- [Ber98] K. Bergmann, H. Theuer and B. W. Shore
Rev. Mod. Phys. **70**(3) 1003–1025 (1998)
DOI: [10.1103/RevModPhys.70.1003](https://doi.org/10.1103/RevModPhys.70.1003)
- [Bre79] E. J. Bredford and F. Engelke

- J. Chem. Phys. **71**(5) 1994–2004 (1979)
DOI: [10.1063/1.438590](https://doi.org/10.1063/1.438590)
- [Bro96] I. N. Bronstein, K. Semendjajew and G. Grosche
Teubner-Taschenbuch der Mathematik
Teubner (1996)
- [COD06] 2006 CODATA recommended values (2006)
<http://physics.nist.gov/cuu/Constants/>
- [Der89] J. Derouard, H. Debontride, T. D. Nguyen and N. Sadeghi
J. Chem. Phys. **90**(11) 5936–5943 (1989)
DOI: [10.1063/1.456360](https://doi.org/10.1063/1.456360)
- [Der01] A. Derevianko, J. F. Babb and A. Dalgarno
Phys. Rev. A **63**(5) 052704 (2001)
DOI: [10.1103/PhysRevA.63.052704](https://doi.org/10.1103/PhysRevA.63.052704)
- [Dij71] H. Dijkerman, W. Flegel, G. Gräff and B. Mönter
Z. Naturforsch. **27a** 100–110 (1971)
- [Doc06] O. Docenko *et al.*
J. Phys. B **39**(19) S929–S943 (2006)
DOI: [10.1088/0953-4075/39/19/S08](https://doi.org/10.1088/0953-4075/39/19/S08)
- [Doc07a] O. Docenko *et al.*
Phys. Rev. A **75**(4) 042503 (2007)
DOI: [10.1103/PhysRevA.75.042503](https://doi.org/10.1103/PhysRevA.75.042503)
- [Doc07b] O. Docenko *et al.*
Phys. Rev. A **75**(5) 059907 (2007)
DOI: [10.1103/PhysRevA.75.059907](https://doi.org/10.1103/PhysRevA.75.059907)
- [Dur74] P. Durand and J. C. Barthelat
Chem. Phys. Lett. **27**(2) 191 – 194 (1974)
DOI: [10.1016/0009-2614\(74\)90201-2](https://doi.org/10.1016/0009-2614(74)90201-2)
- [Dur75] P. Durand and J.-C. Barthelat
Theor. Chim. Acta **38**(4) 283–302 (1975)
DOI: [10.1007/BF00963468](https://doi.org/10.1007/BF00963468)
- [Dur92] G. Durand
Manuel d'utilisation des programmes
Laboratoire de Physique Quantique, IRSAMC (1992)

- [Eva83] S. Evangelisti, J.-P. Daudey and J.-P. Malrieu
Chem. Phys. **75** 91 – 102 (1983)
DOI: [10.1016/0301-0104\(83\)85011-3](https://doi.org/10.1016/0301-0104(83)85011-3)
- [Fal06a] S. Falke, I. Sherstov, E. Tiemann and C. Lisdat
J. Chem. Phys. **125**(22) 224303 (2006)
DOI: [10.1063/1.2375120](https://doi.org/10.1063/1.2375120)
- [Fal06b] S. Falke *et al.*
Phys. Rev. A **74**(3) 032503 (2006)
DOI: [10.1103/PhysRevA.74.032503](https://doi.org/10.1103/PhysRevA.74.032503)
- [Fal07] S. Falke
High Precision Spectroscopy on Beams of Atoms and Dimers
Ph.D. thesis, IQO Hannover (2007)
- [Fer00] R. Ferber *et al.*
J. Chem. Phys. **112**(13) 5740–5750 (2000)
DOI: [10.1063/1.481149](https://doi.org/10.1063/1.481149)
- [Fou92] M. Foucrault, P. Millie and J. P. Daudey
J. Chem. Phys. **96**(2) 1257–1264 (1992)
DOI: [10.1063/1.462162](https://doi.org/10.1063/1.462162)
- [Ger08] A. Gerdes, M. Hobein, H. Knöckel and E. Tiemann
Eur. Phys. J. D **49**(1) 67–73 (2008)
DOI: [10.1140/epjd/e2008-00138-7](https://doi.org/10.1140/epjd/e2008-00138-7)
- [Gue09] R. Guerout, F. Spiegelman and O. Dulieu
To be published (2009)
- [HCN97] Hochspannungs - Netzgeräte, HCN-Serie
Betriebsanleitung (1997)
- [Her50] G. Herzberg
Spectra of diatomic molecules
Van Nostrand Reinhold Company Inc. (1950)
- [Hob06] M. Hobein
Fourier Transform Spectroscopy on Polar Alkali Dimers
Diploma thesis, IQO Hannover (2006)
- [Hur73] B. Huron, J. P. Malrieu and P. Rancurel
J. Chem. Phys. **58**(12) 5745–5759 (1973)
DOI: [10.1063/1.1679199](https://doi.org/10.1063/1.1679199)

- [Ish94] K. Ishikawa, N. Mukai and M. Tanimura
J. Chem. Phys. **101**(2) 876–881 (1994)
DOI: [10.1063/1.467740](https://doi.org/10.1063/1.467740)
- [Jen97] P. Jensen
Einführung in die Methoden der Quantenchemie
Bergische Universität Wuppertal (1997)
- [Jun06] S. Jung
*Erzeugung kalter SO₂ Moleküle zur Untersuchung ihrer
schwelnahen Photodissoziation*
Ph.D. thesis, IQO Hannover (2006)
- [Kas91] S. Kasahara, M. Baba and H. Katô
J. Chem. Phys. **94**(12) 7713–7720 (1991)
DOI: [10.1063/1.460157](https://doi.org/10.1063/1.460157)
- [Kas09] S. Kasahara
Private communication, raw input data of [kat90] (2009)
- [Kat90] H. Katô *et al.*
J. Chem. Phys. **93**(4) 2228–2237 (1990)
DOI: [10.1063/1.459056](https://doi.org/10.1063/1.459056)
- [Knö09] H. Knöckel
Private communication (2009)
- [Kot00] S. Kotochigova, E. Tiesinga and P. S. Julienne
Phys. Rev. A **63**(1) 012517 (2000)
DOI: [10.1103/PhysRevA.63.012517](https://doi.org/10.1103/PhysRevA.63.012517)
- [LB04] H. Lefebvre-Brion and R. W. Field
The Spectra and Dynamics of Diatomic Molecules
Elsevier (2004)
- [LeR74] R. J. LeRoy
Can. J. Phys. **52** 246–256 (1974)
- [Lis01a] C. Lisdat
*Realisation eines Materiewelleninterferometers für Moleküle
und neue Möglichkeiten zur Beobachtung von Atom-
Molekül-Stößen*
Ph.D. thesis, IQO Hannover (2001)

- [Lis01b] C. Lisdat, O. Dulieu, H. Knöckel and E. Tiemann
Eur. Phys. J. D **17**(3) 319–328 (2001)
DOI: [10.1007/s100530170006](https://doi.org/10.1007/s100530170006)
- [Mar99] M. Marinescu and H. R. Sadeghpour
Phys. Rev. A **59**(1) 390–404 (1999)
DOI: [10.1103/PhysRevA.59.390](https://doi.org/10.1103/PhysRevA.59.390)
- [Mue84] W. Mueller, J. Flesch and W. Meyer
J. Chem. Phys. **80**(7) 3297–3310 (1984)
DOI: [10.1063/1.447083](https://doi.org/10.1063/1.447083)
- [Nes63] A. Nesmeyanov
Vapor pressure of the chemical elements
Elsevier (1963)
- [Ni08] K.-K. Ni *et al.*
Science Express **1** 1–6 (2008)
- [Pas00] A. Pashov
Laser spectroscopy of selected excited electronic states of alkali metal diatomic molecules
Ph.D. thesis, Polish Academy of Sciences (2000)
- [Pas07] A. Pashov *et al.*
Phys. Rev. A **76**(2) 022511 (2007)
DOI: [10.1103/PhysRevA.76.022511](https://doi.org/10.1103/PhysRevA.76.022511)
- [Pil01] F. L. Pilar
Elementary quantum chemistry
Dover (2001)
- [Por03] S. G. Porsev and A. Derevianko
J. Chem. Phys. **119**(2) 844–850 (2003)
DOI: [10.1063/1.1578052](https://doi.org/10.1063/1.1578052)
- [RA00] I. Russier-Antoine *et al.*
J. Phys. B **33**(14) 2753–2762 (2000)
DOI: [10.1088/0953-4075/33/14/312](https://doi.org/10.1088/0953-4075/33/14/312)
- [Ros85] C. Ross, A. J. and Effantin, J. d’Incan and R. F. Barrow
Mol. Phys. **56**(4) 903–912 (1985)
DOI: [10.1080/00268978500102791](https://doi.org/10.1080/00268978500102791)

- [Ros86] A. J. Ross and G.-H. Jeung
Chem. Phys. Lett. **132**(1) 44–49 (1986)
DOI: [10.1016/0009-2614\(86\)80691-1](https://doi.org/10.1016/0009-2614(86)80691-1)
- [Ros88] A. J. Ross, R. M. Clements and R. F. Barrow
J. Mol. Spectr. **127**(2) 546 – 548 (1988)
DOI: [10.1016/0022-2852\(88\)90142-7](https://doi.org/10.1016/0022-2852(88)90142-7)
- [Ros08] A. Ross
Private communication (2008)
- [Sal09] H. Salami *et al.*
Phys. Rev. A **80**(2) 022515 (2009)
DOI: [10.1103/PhysRevA.80.022515](https://doi.org/10.1103/PhysRevA.80.022515)
- [Sam03] C. Samuelis *et al.*
Eur. Phys. J. D **26**(3) 307–318 (2003)
DOI: [10.1140/epjd/e2003-00294-2](https://doi.org/10.1140/epjd/e2003-00294-2)
- [Sco88] G. Scoles
Atomic and Molecular Beam Methods
Oxford University Press (1988)
- [Shu59] H. Shull and G. G. Hall
Nature **184** 1559–1560 (1959)
DOI: [10.1038/1841559a0](https://doi.org/10.1038/1841559a0)
- [Sla30] J. C. Slater
Phys. Rev. **36**(1) 57–64 (1930)
DOI: [10.1103/PhysRev.36.57](https://doi.org/10.1103/PhysRev.36.57)
- [Smi65] B. Smirnov and B. Chibisov
Sov. Phys. JETP **21** 624 (1965)
- [Sta05] C. A. Stan and W. Ketterle
Rev. Sci. Instr. **76**(6) 063113 (2005)
DOI: [10.1063/1.1935433](https://doi.org/10.1063/1.1935433)
- [Ste06] A. Stein
Auswertung großer Datenmengen aus der Fourier-Transform-Spektroskopie von Molekülen
Diploma thesis, IQO Hannover (2006)
- [Stu05] J. Stuhler *et al.*

- Phys. Rev. Lett. **95**(15) 150406 (2005)
DOI: [10.1103/PhysRevLett.95.150406](https://doi.org/10.1103/PhysRevLett.95.150406)
- [Sza96] A. Szabo and N. S. Ostlund
Modern Quantum Chemistry
Dover Publications (1996)
- [Tan84] K. T. Tang and J. P. Toennies
J. Chem. Phys. **80**(8) 3726–3741 (1984)
DOI: [10.1063/1.447150](https://doi.org/10.1063/1.447150)
- [Tow75] C. H. Townes and A. Schawlow
Microwave spectroscopy
Dover Publications, New York (1975)
- [Ven01] V. Venturi, M. J. Jamieson and R. Côté
J. Phys. B **34**(22) 4339–4347 (2001)
DOI: [10.1088/0953-4075/34/22/305](https://doi.org/10.1088/0953-4075/34/22/305)
- [vV65] J. van Vleck
The theory of electric and magnetic susceptibilities
Oxford University Press (1965)
- [Wei99] J. Weiner, V. S. Bagnato, S. Zilio and P. S. Julienne
Rev. Mod. Phys. **71**(1) 1–85 (1999)
DOI: [10.1103/RevModPhys.71.1](https://doi.org/10.1103/RevModPhys.71.1)
- [Wie99] C. E. Wieman, D. E. Pritchard and D. J. Wineland
Rev. Mod. Phys. **71**(2) S253–S262 (1999)
DOI: [10.1103/RevModPhys.71.S253](https://doi.org/10.1103/RevModPhys.71.S253)
- [Win06] LINOS WinLens software
<http://www.opticalsoftware.net/>
- [Wor81] R. F. Wormsbecher, M. M. Hessel and F. J. Lovas
J. Chem. Phys. **74**(12) 6983–6985 (1981)
DOI: [10.1063/1.441067](https://doi.org/10.1063/1.441067)
- [Zem99] W. T. Zemke and W. C. Stwalley
J. Chem. Phys. **111**(11) 4956–4961 (1999)
DOI: [10.1063/1.479782](https://doi.org/10.1063/1.479782)
- [Zep09] M. Zeppenfeld, M. Motsch, P. W. H. Pinkse and G. Rempe
Phys. Rev. A **80**(4) 041401 (2009)
DOI: [10.1103/PhysRevA.80.041401](https://doi.org/10.1103/PhysRevA.80.041401)

CURRICULUM VITAE

Andreas Gerdes

Personal data

Date of Birth:	18.04.1978
Place of Birth:	Wilhelmshaven
Nationality:	German
Marital status:	Single
Email:	andreas.gerdes@email.de

Studies

09/2005 to date	PhD student and scientific coworker in the group of Prof. E. Tiemann Institute of quantum optics, University of Hannover
12/2004 - 07/2005	Scientific coworker Institute of solid state physics, Univer- sity of Hannover Surface department
10/2001 - 11/2004	Physics - University of Hannover Qualification: Diplom
10/1999 - 09/2001	Physics - Humboldt-University Berlin Qualification: Vordiplom

Scholarships	
2005 - 2008	Scholar of the European Graduate College 665 (DFG) Interference and quantum applications
2001 - 2004	Full scholarship of the Studienstiftung des deutschen Volkes

Talents	
Music	Classical music, playing the piano, singing in choirs
Sports	Running (Half marathon), Dancing
Miscellaneous	Linux, internet technologies, classical literature, note engraving with Lily- Pond

PUBLICATIONS

List of publications in chronological order:

J. Wollschläger, C. Deiter, M. Bierkandt, A. Gerdes, M. Bäumer, C.R. Wang,
B.H. Müller and K.R. Hofmann
*Homogeneous Si films on CaF₂/Si(111) due to boron enhanced
solid epitaxy*
Surf. Sci. **600** 3637-3641 (2006)

A. Gerdes, M. Hobein, H. Knöckel and E. Tiemann
Ground state potentials of the NaK molecule
Eur. Phys. J. D **49**(1) 67-73 (2008)
DOI: [10.1140/epjd/e2008-00138-7](https://doi.org/10.1140/epjd/e2008-00138-7)
The original publication is available at www.epj.org

M. Aymar, N. Bouloufa, J. Deiglmayr, A. Gerdes and O. Dulieu
*Full set of potential energy curves and transition dipole moment func-
tions for the Cs dimer*
J. Chem. Phys.
To be published

